Quorum-Sensing Control of the Chromobacterium vaccinii Volatilome: A Molecular Genetic Study Enabled by Custom Image Analysis

By

Victor Quarterone do Prado

BS, University of Illinois at Urbana-Champaign, 2023

Thesis

Submitted in partial fulfillment of the requirements for the Degree of Master of Science in the Graduate Program of Biotechnology at Brown University

PROVIDENCE, RHODE ISLAND

May 01, 2026

AUTHORIZATION TO LEND AND REPRODUCE THE THESIS

As the sole author of this thesis, I authorize Brown University to lend it to other institutions for the purpose of scholarly research.

Date__May 01, 2026________ ____

Victor Quarterone do Prado, Author

I further authorize Brown University to reproduce this thesis by photocopying or other means, in total or in part, at the request of other institutions or individuals for the purpose of scholarly research.

Date__May 01, 2024________ ____

Victor Quarterone do Prado, Author

This thesis by Victor Quarterone do Prado is accepted in its present form by the Graduate Program in Biotechnology as satisfying the thesis requirements for the degree of Master of Science

Date_______________ Signature: ___________________________________

Dr. Gerard J. Nau, Advisor

Date_______________ Signature: ___________________________________

Dr. Adam Crego, Reader

Date_______________ Signature: ___________________________________

Dr. Christina Cuomo, Reader

Approved by the Graduate Council

Date_______________ Signature: ___________________________________

David P. Lindstrom, Dean of the Graduate School

Acknowledgments

I would like to express my sincere gratitude to my mentor and advisor, Dr. Gerard J. Nau, for his guidance, intellectual generosity, and unwavering support throughout the course of this work. His passion for science and willingness to engage with the questions that drove this research have shaped both this thesis and my development as a scientist in ways I will carry forward well beyond graduate school. I would also like to acknowledge the efforts of Alexis Jacober and Nikolas Montaquila, whose foundational laboratory work provided a basis for the biological investigation presented in Chapter 3. This thesis would not have taken the shape it did without the careful and dedicated work they have done for the Nau laboratory. To my labmates and my family, thank you for the support throughout this process. Thank you for being there for me when I didn't even know how much your help and comfort was needed.

Table of Contents

Table of Figures

Table of Tables

Abstract of Quorum-Sensing Control of the Chromobacterium vaccinii Volatilome: A Molecular Genetic Study Enabled by Custom Image Analysis, by Victor Quarterone do Prado, ScM, Brown University, May, 2026.

The quantification of microbial colony growth on solid media is currently compromised by a mismatch between the assumptions embedded in common biological image analysis tools and the imaging properties of petri dish images. These platforms were optimized for mammalian cell microscopy workflows and fail in three specific ways when applied to plate-based assays: intensity-based object identification logic misclassifies artifacts as biological objects, shape-based declumping algorithms fragment identified colonies, and the absence of any filtering allows noise to propagate and skew measurement outputs. This thesis addresses this translational gap and applies the resulting analysis framework to a molecular investigation of the regulatory mechanisms governing the volatile-mediated antifungal activity in *Chromobacterium vaccinii*. Four converging angles of genetic and pharmacological evidence establish that volatile inhibition of *C. albicans* by *C. vaccinii* is independent from the biosynthesis of the known antibiotic purple pigment produced by the bacteria, violacein, and strictly requires a functional CviR quorum sensing receptor to exhibit significant activity. Pigment-null strains of *C. subtsugae* and *C. vaccinii* were shown to retain equal inhibitory capacity, while a quorum sensing mutant of *C. vaccinii* failed to inhibit growth of *Candida albicans* to an extent indistinguishable from an uninhibited control. These findings set quorum sensing as the primary regulatory mechanism for the volatile antifungal output of *C. vaccinii* and narrow the candidate active compounds to the non-violacein fraction of CviR-regulated secondary metabolites, with relevance to antifungal drug discovery targeting priority fungal pathogens.

Chapter 1: General Introduction

Quantitative microbiology depends on the ability to translate visual biological behaviour into well-defined, reproducible data. Whether the goal is to characterize the competitive fitness of mutant strains or map the morphological effects of environmental stress, biological conclusions are only as valid as the measurements derived from them. This thesis originates from precisely that dependency. The biological investigation at its center focuses on understanding the regulatory mechanisms governing the volatile-mediated antifungal activity of *Chromobacterium vaccinii*, and it required the quantification of fungal colony growth across a set of experimental conditions with sufficient precision to reliably report extreme ranges in colony growth rather than simple binary or qualitative outcomes. When existing automated tools proved inadequate for that specific imaging context, the development of a specialized pipeline became not a parallel project but a prerequisite. The result is two interconnected sections within this body of work: the development and validation of a colony analysis pipeline designed specifically for plate-based microbial imaging, and the biological investigation that motivated it and showcases its practical relevance.

The automated tools most widely available for this purpose were not primarily designed with plate-based microbiology in mind. The dominant platforms for biological image analysis were developed for mammalian cell microscopy, and their adoption into plate-based microbiology carries assumptions about imaging scale and object geometry that do not straightforwardly transfer [1–3]. More broadly, these platforms are distributed as flexible, modular frameworks in which pipeline configuration is expected to be adjusted on a per-experiment basis to better capture the specific imaging conditions at hand. In the context for which these tools were designed, where microscopy images might greatly differ from one another across experiments, that flexibility is an intended feature. In the context of plate-based microbiology, specifically when handling a single species or a subset of highly similar colonies of organisms, it introduces a potential weakness: the parameter choices governing what gets identified as a biological object, or discarded as noise, are made during a process that is not isolated from knowledge of the expected experimental outcome, and are rarely disclosed in sufficient detail for independent replication. This is most consequential under conditions of sparse and attenuated growth, where small, faint colonies are poorly differentiable from their background. It is precisely under these conditions, which the biological problem at the core of this thesis extensively deals with, that current tools are most likely to either miss genuine biological signals entirely or incorporate background noise at unacceptable rates into their measurements. Addressing this gap requires tools whose malleability and recalibration are controlled, whose design choices are transparent, and whose performance has been empirically validated against independently-defined ground truth in the specific imaging context where they will be applied.

Beyond the methodological gap just described, the biological problem belongs to a broader scientific space facing a distinct, yet more dire, challenge. Invasive fungal infections represent a significant and growing burden on global public health, disproportionately affecting immunocompromised populations for whom treatment options are severely scarce. In 2022, the World Health Organization issued a priority list of fungal pathogens formalizing the urgency of this problem, identifying a panel of species for which future development of novel antifungal interventions should prioritize [4]. All four individuals placed in the highest priority level of this list, *Candida albicans*, *Candida auris*, *Aspergillus fumigatus*, and *Cryptococcus neoformans* have been shown, by unpublished data in the Nau laboratory, to be susceptible to Chromobacteria-emitted volatile organic compounds. The fungal model organism addressed in this thesis is within that top four global health critical priority targets, *Candida albicans*, chosen as the focus of this research as it is the most common causative agent of invasive candidiasis worldwide [5]. This growing burden is in part caused by the scarcity of available pharmacological agents for antifungal therapy and reflects a fundamental constraint: fungi are eukaryotic organisms that share substantial cellular processes with human hosts, restricting the number of molecular targets that antifungal compounds can selectively exploit [6]. The drug classes that do currently exist face mounting resistance pressure from clinically relevant pathogens, and the development of genuinely novel antifungal agents has not kept pace with clinical need [6]. In light of these facts, the volatile metabolomes of certain bacteria offer a mechanistically distinct and largely underexplored avenue for antifungal discovery [7]. Bacteria have evolved sophisticated strategies for suppressing microbial competitors across ecological niches, and gas-phase metabolites, volatile organic compounds capable of diffusing through the environment and inhibiting microbial competitors without any direct contact, are increasingly recognized- largely outside of the medical field- as a potent and widespread alternative to this problem. While much of microbiology has worked on the mechanisms of contact-dependent and diffusible antimicrobial activity, the responsible genes, gene-products, and regulatory machinery governing volatile-mediated activity remain largely uncharacterized across bacterial taxa.

So, this work studies the volatilome of individuals in the Chromobacterium genus. *Chromobacterium vaccinii*, a Gram-negative environmental isolate seen to reproducibly and substantially suppress the growth of clinically relevant fungal pathogens through volatile emissions [7], serves as the model organism for this investigation. Dissecting the regulatory mechanisms underlying this activity requires the ability to detect subtle phenotypic shifts, not merely counting colonies, capturing high-fidelity measurements of growth area that can distinguish between a wild-type response and a partially attenuated mutant.

The development and rigorous validation of a purpose-built quantification pipeline is therefore not a preliminary step but a prerequisite for the biological investigation that follows, and the reliability of the biological conclusions presented in this thesis is directly bound by the quality of the evidence supporting the developed measurement tool and of the evidence generated by said tool. Chapter 2 demonstrates that this custom-built pipeline achieves a mean segmentation fidelity score approximately threefold greater than the most directly comparable existing pipeline identified, with a near-zero count bias of +1.5 colonies per image, species invariant performance across both *Candida albicans* and *Staphylococcus aureus*, and identification stability under increasing colony crowding. Chapter 3 then applies this validated framework to establish that volatile-mediated antifungal activity in *C. vaccinii* is independent of violacein and requires a functional CviR quorum sensing receptor to meaningfully activate production of active volatile organic compounds and significantly stun fungal development. Neither chapter stands fully on its own. The biological discoveries of Chapter 3 are credible precisely because of the validation program of Chapter 2, and the practical significance of what is presented in Chapter 2 is demonstrated by enabling the biological question explored in Chapter 3.

Chapter 2: Development and Validation of a Semi-Automated Image Analysis Pipeline for Microbial Colony Quantification

Introduction

The automated or semi-automated quantification of microbial growth on solid media is frequently compromised in current publicly available workflows by a fundamental mismatch between image analysis algorithms and the optical profiles of petri dish imaging [8]. Tools such as ImageJ and OpenCFU laid the foundations for modern computational phenotyping by making digital measurements accessible to non-specialist researchers, and dedicated colony-counting tools have more recently been developed to address this application specifically [9–11]. CellProfiler, on that note, has become one of the most widely adopted platforms for biological image analysis [1,2,12]. However, CellProfiler was originally designed and optimized for small, discrete, individually resolvable objects contrasted by clean, low-noise backgrounds typical of fluorescently stained cells under a microscope objective [1,3,13,14]. Plate-based colony assays differ from this microscopy substantially. A manual review of the software's official documentation reveals that only 5% of all its applications target plate-based assays, reflecting a deep algorithmic orientation toward the micro-scale that often fails when confronted with the macro-scale characteristics of a petri dish [1,15].

These failures arise from three specific properties of the standard pipeline logic. First, core object identification relies heavily on intensity-based thresholding, which operates on a binary logic that classifies any pixel exceeding a specific brightness as a valid object. In the complex setting of a petri dish, this logic commonly recognizes non-biological artifacts, such as light reflections, condensation droplets, and agar irregularities, as desired objects alongside genuine growth. Second, shape-based segmentation algorithms attempt to resolve touching objects by recognizing and estimating boundaries at local intensity minima, a strategy calibrated for the well-defined, often stained compartments of individual eukaryotic cells. When applied to microbial colonies, this misinterprets internal surface variation as inter-object boundaries, colonies are fragmented into "shattered" digital representations, inaccurately reporting parameter values crucial to microbiology studies. Third, standard pipelines lack any biological plausibility filter. Artifacts pass directly into measurement outputs alongside genuine colonies, inflating counts and area estimates by orders of magnitude. In studies requiring the detection of subtle phenotypic differences, as is the case for the experimental work in Chapter 3, the accumulation of such false positives introduces statistical noise severe enough to obscure genuine biological effects entirely.

To address these limitations, a custom image analysis pipeline was developed using CellProfiler (version 4.2.8) specifically for quantification of microbial colony growth on solid media, named the Colony Analysis and Morphometry Pipeline (CAMP) [1–3,12]. Rather than relying on complex, independent all-in-one modules, this workflow decomposes object identification into a series of transparent, modular processing steps. The pipeline employs two pre-configured workflow branches best suited for the extremes of intensity distributions across an image, modular segmentation algorithms also pre-determined based on extreme image conditions, and a set of mathematically-based filtering parameters, eccentricity, solidity, compactness, and extent, that distinguish true biological growth- single or clustered- from background noise based on colony-specific structural features or extreme non-biological properties of objects.

The performance of CAMP was evaluated against two established comparator workflows to provide a comprehensive benchmark of current capabilities. The first, the official CellProfiler Yeast Template pipeline, represents the most direct application of the software's recommended logic to colony phenotyping, produced directly by the developers of the software [15]. The second comparator, hereafter referred to as the Choudhry pipeline, is a CellProfiler pipeline from a publicly available, peer-reviewed paper [16]. It was selected because the author conducted an extensive review on the efficacy of existing automated tools in a variety of tasks, including microbial colony quantification, within their work (12). Hence, their implementation serves as a credible representation of the standard pipelines currently available to the scientific community for this type of analysis. Evaluation of the developed pipeline proceeded in two complementary stages. The first benchmarked all three pipelines against expert-annotated ground truth on a subset of 100 real petri dish images from the AGAR (Annotated Germs for Automated Recognition) dataset, containing representatives of either *Candida albicans* and *Staphylococcus aureus* [17]. This stage assessed performance across dimensions including: pixel-level segmentation fidelity, object identity resolution, and colony count accuracy.

The second stage addressed the high sensitivity of the comparator pipelines to colony density. While these tools may work reliably with abundant foreground signals, their performance often collapses on sparse or highly crowded plates. Sparse conditions were thoroughly addressed with the 100 AGAR images, but they lacked substantial representation of objectively "dense" colony growth. Because density is broadly used to describe both the total amount of biological signal and the degree of inter-colony overlap, this study decoupled these two factors through a controlled synthetic validation to isolate cases of increasing colony-overlap [18]. By transposing colonies from the AGAR dataset, through a mathematically controlled manner, into image sets of low, moderate, and high-overlap degrees, synthetic plates were generated that retain biological authenticity while providing absolute ground-truth data. This framework allows for a more rigorous evaluation of CAMP against the comparators as spatial crowding increases. The results demonstrate the strength in algorithmic adaptability over the intended pipeline configuration flexibility where comparators not only fail to identify colonies over increasing crowding, they fundamentally misinterpret the biological truth. Ultimately, their analysis of images lead to skewed core colony characteristics to a degree that would compromise downstream experimental conclusions.

Materials and Methods

Software Environment and Computational Platform

All image analysis was performed using CellProfiler version 4.2.8, an open-source platform for high-throughput phenotypic image analysis developed at the Broad Institute [1–3,12]. Three pipelines were implemented and compared: CAMP developed in the present work, the CellProfiler Template pipeline, and the Choudhry pipeline. Their key architectural properties are summarized in Table 1. Pipelines were constructed, executed, and validated within the CellProfiler graphical user interface on a Windows workstation. Measurement outputs were exported directly from CellProfiler to comma-separated value spreadsheets for downstream statistical analysis.

Property	**CAMP**	**CellProfiler Template Pipeline**	**Choudhry (2016) Pipeline**
Total modules	48	23	28
Detection strategy	Threshold → Filter → Watershed/Segmentation	IdentifyPrimaryObjects (single module)	IdentifyPrimaryObjects (single module)
Thresholding method	Otsu (Large) / Adaptive MCE (Small)	Min. Cross-Entropy (global)	Otsu with log-transform (global)
Morphological filter	FilterObjects: 4–5 criteria	None	FilterObjects: FormFactor + MaxRadius

Object diameter range	Unconstrained	1–40 px	2–20 px
Watershed segmentation	Marker-seeded (FindMaxima + Watershed)	Shape-based (internal to IPO)	None
Architecture	Dual-branch (Large + Small)	Single-pass	Single-pass

Table 1. Summary comparison of the three pipeline architectures.

Image Processing

One hundred annotated plate images were drawn from the AGAR (Annotated Germs for Automated Recognition) dataset, comprising 54 *Candida albicans* and 46 *Staphylococcus aureus* images, with candidates excluded only if they contained contamination or mixed morphologies [17]. Each image in the AGAR dataset contains its own independently-annotated individual colony boundaries, which were used as the unbiased ground truth for all colony quantification performance evaluations.

Synthetic images were generated using a patch-based compositing approach adapted from the Pawlowski research group, who demonstrated that realistic, fully annotated synthetic colony images can be produced from the AGAR dataset through a combination of neural style transfer and colony patch compositing [18]. The original implementation was modified to introduce experimental control over inter-colony overlap as an adjustable parameter, enabling the generation of three distinct overlap conditions. All colony patch source material was drawn from the same 100 AGAR benchmark images used for performance measurements, ensuring direct morphological and imaging continuity between the naturally and synthetically obtained datasets. Colony patches were extracted from the AGAR dataset annotations using per-colony bounding box coordinates and organized into libraries. Each patch was processed to produce smooth, naturalistic colony boundaries through color and edge blending with background.

Three overlap conditions were created by varying two parameters simultaneously: an overlap threshold controlling the maximum degree of overlap and the number of patches placed per cluster. Set 1 used a strict rejection threshold with low colony density, at 10% overlap with 40-60 colonies per cluster. Set 2 had a more permissive threshold limit with higher colony density, at 30% overlap with 90-110 colonies per cluster. Lastly, Set 3 had the most permissive threshold with the highest colony density, at 50% overlap and 140-160 colonies per cluster. Fifty images per species were generated per overlapping condition (300 total images).

Prior to CellProfiler analysis, images were preprocessed by a Hough-circle transformation to isolate the circular agar surface and remove surrounding background, generating standardized plate images as pipeline inputs [8]. Ground-truth colony area for each placed patch was recorded at the moment of placement, and their per-image collection constitutes the ground-truth size distribution against which all pipeline outputs were compared in the distributional fidelity analysis. The transformation parameters relating original image coordinates to the standardized output were saved as per-image metadata for use in downstream synthetic image construction.

All three pipelines share an identical preprocessing sequence prior to their respective colony identification strategies. RGB images are converted to grayscale, downsampled to 25% of original linear dimensions, spatially standardized via a coordinate-based crop, corrected for uneven illumination (polynomial fitting, per-image cycle), and intensity-normalized to and capped to the 0.0 to 1.0 range. The output of this shared sequence serves as input to each pipeline's segmentation modules.

Pipeline Architectures

CAMP functions by analyzing each image through two independent lenses or branches, one optimized for images with abundant colony growth (large branch) and one for images with sparse or phenotypically attenuated growth (small branch). Both branches stem from the same preprocessing sequence described in the previous sub-section and differ in their thresholding strategy, filter parameter settings, and declumping parameters, reflecting the distinct imaging characteristics of dense versus sparse colony distributions.

In the large branch, illumination correction uses the "Regular" method with polynomial fitting, which estimates the illumination function from the full foreground signal rather than background alone. Following rescaling, a global thresholding is applied to produce a binary foreground mask of labeled objects. Candidate objects are measured for morphometric properties before being subjected to the four-criteria filter: solidity ≥ 0.3, eccentricity ≤ 0.95, compactness ≥ 0.6, and extent ≥ 0.3. Objects failing any criterion are excluded and retained as a removed-objects class for output review. Validated objects then serve as seed, or object center, candidates for object segmentation, in which local intensity textures are analyzed to determine how objects of unique centers should be segmented, leading to the assignment of all foreground pixels into groups reflecting real colonies.

The small branch follows the same logical sequence as the large branch but it follows an adaptive thresholding strategy rather than global, and applies a five-criteria filter that adds a minimum intensity criterion (MaxIntensity ≥ 0.1) to the filtering step. The minimum compactness value of the small branch is lowered to 0.3 (compared to 0.6 in the other branch), reflecting greater imaging irregularity of faint or attenuated colonies at the downsampled image resolution. Furthermore, seeding density parameters are reduced to accommodate the smaller typical colony size under sparse-growth conditions.

The CellProfiler Template pipeline carries out all object detection with a single all-in-one module, "IdentifyPrimaryObjects." This module handles object detection with a global thresholding strategy, limited to an object diameter range of 1-40 pixels, and segmenting objects by shape-based declumping distinction alone. All detected objects passing the diameter criterion are forwarded directly to measurement without further filtering. The Choudhry pipeline implements the method described by Choudhry (2016) for high-throughput colony and cell counting by digital image analysis [16]. Following the shared preprocessing sequence it employs the same all-in-one module used by the CellProfiler Template pipeline for detection, using global thresholding applied after a logarithmic intensity transformation, with an object diameter range of 2-20 pixels. Detected candidates are filtered using two criteria: a minimum "FormFactor" of 0.2, enforcing a minimum degree of circularity, and a minimum "MaximimRadius" of 2.0 pixels, excluding spotted noise.

Apart from modules needed for detection, identification, and quantification, modules were also added for comparison between ground-truth values and experimentally-determined values. These modules determine pixel-level F-factor and Adjusted Rand Index scores, enabling direct evaluation of colony recognition alongside segmentation accuracy analysis.

Pipeline Validation

Pipeline outputs for each of the 100 benchmark images were evaluated against the AGAR ground-truth annotations using degree of overlap modules within CellProfiler, which computes pixel-level agreement between a predicted foreground mask and a reference mask. The following metrics were extracted for each pipeline-image pair: the F-factor (harmonic mean of pixel-level precision and recall), the Adjusted Rand Index (ARI), the mean of all morphometric parameters considered for filtering in CAMP, and the total area occupied by detected objects. Colony counts were extracted from the object count output of the respective detection modules. All measurements were exported via CellProfiler and compiled into a structured dataset for statistical analysis.

Pipeline performance metrics were compared using a non-parametric approach throughout: Spearman rank correlation (ϱ). All statistical analyses were performed through Graphpad Prism or R. For the synthetic images, individual colony area values were extracted per pipeline per image from exporting modules and compiled into species-stratified datasets (50 images per species per set). To characterize the distributional behavior of each pipeline across overlap conditions, five summary metrics were computed per pipeline per set: median detected colony size, modal peak location, mean detected objects per image, percentage of detections below the first quartile of the ground-truth control distribution, and the percentage of detections within the interquartile range of the ground-truth control distribution. The lower and upper zone thresholds used in the latter two metrics were defined as the first and third quartiles of the colony size distribution from the ground-truth control across the three sets. These values were Q_1 = 107 pixels and Q_3 = 207 pixels. This approach anchors the zone boundaries to the reference distribution itself, such that objects below Q_1 represent detections in the lower tail of the normal colony size range and objects within the interquartile range represent the central 50% of biologically typical colony sizes as defined by the ground truth.

Results

Pixel-level Fidelity and Colony Resolution

Across the full 100 images subset, CAMP achieved a mean F-factor of 0.779 (± 0.050 SD, range 0.666–0.884), reflecting a consistently high colony boundary match with the annotated ground truth. By contrast, the CellProfiler Template pipeline exhibited a mean F-factor of 0.281 (± 0.370

SD, range 0.000–0.851), with a distribution heavily skewed toward low values (median = 0.027). The Choudhry pipeline demonstrated substantially lower accuracy, yielding a mean F-factor of 0.039 (± 0.075 SD, median = 0.012), indicating a complete loss of specificity under these imaging conditions (Figure 1A). When F-factor scores were stratified by species (Figure 1B), CAMP demonstrated stable accuracy across both representative species, recording a mean of 0.763 (± 0.045) for *C. albicans* and 0.797 (± 0.051) for *S. aureus*. The CellProfiler Template pipeline, which was originally designed and optimized for yeast colony analysis, exhibited a markedly greater species-dependent performance drop: its mean F-factor for *C. albicans* (0.357 ± 0.384) was substantially higher than that observed for *S. aureus* (0.193 ± 0.334), reflecting that its segmentation logic is largely non-transferable to morphologically distinct organisms.

Representative CellProfiler output panels for an example *Candida albicans* image showing the unadulterated plate image, detected objects, and detection overlay for both CAMP (specific F-factor of 0.796) and the CellProfiler Template pipeline (specific F-factor of 0.008) consolidates the practical differences in F-factor scores (Appendix Figures A1 and A2). At 0.796, CAMP correctly identifies the sparse faint colonies visible on the plate with only minor boundary discrepancies, whereas CellProfiler Template pipeline, at 0.008, utterly fails to identify and set colony boundaries.The resulting objects produced by the comparator pipeline are fragmented artifactual detections that span even the plate rim, consistent with the skewed geometric values approaching or reaching biologically-implausible ranges (Figure 6).

The Adjusted Rand Index (ARI), which quantifies the degree to which groups of pixels are correctly bound to their respective true biological colonies rather than merged artifacts or fragmented noise, was computed for all pipeline-image pairs (Figure 1C). CAMP achieved a mean ARI of 0.777 (± 0.050), closely paralleling its F-factor performance and indicating that detected objects were consistently resolved as accurate representations of the given true colonies. The

Cellprofiler Template pipeline and the Choudhry pipeline recorded mean ARI values of 0.276 (± 0.370) and 0.030 (± 0.073), respectively, with the majority of individual scores clustering near zero (Figure 1C).

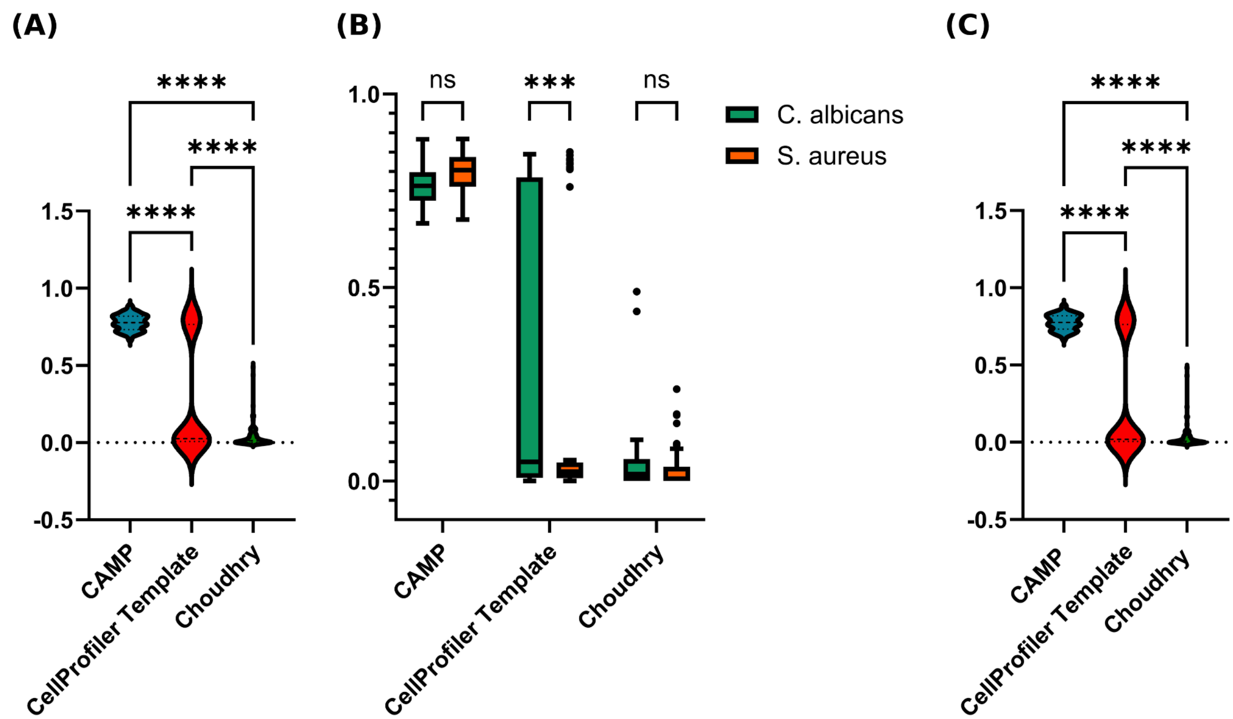

Figure 1. F-factor and ARI across all 100 AGAR benchmark images. (A) F-factor distributions per pipeline. (B) F-factor stratified by species. (C) Adjusted Rand Index distributions. CAMP achieves mean F-factor - 0.779 and ARI = 0.777; CellProfiler Template Pipeline and Choudhry record means of 0.281/0.276 and 0.039/0.030 respectively.

Quantified Colony Features

Colony Count accuracy was evaluated by plotting pipeline-predicted counts against AGAR ground-truth annotations on a 1:1 identity reference line (Figure 2A). CAMP demonstrated near-perfect agreement with the ground truth, with predicted counts ranging from 1 to 69 (mean = 15.3. Both comparator pipelines exhibited marked and consistent overcounting. The CellProfiler Template pipeline predicted between 0 and 2,229 colonies per image (mean = 1,013.4), while the

Choudhry pipeline returned counts ranging from 3 to 1,057 per image (mean = 572.1), in both cases producing values orders of magnitude above of the annotated ground truth (Figure 2A). The progressive divergence from the identity line with increasing ground-truth colony number, particularly in the CellProfiler Template pipeline output, indicates compounding of suboptimally-ran operations (faulty detection followed by faulty segmentation of detected objects) rather than simple proportional error. Bland-Altman analysis of count agreement confirmed the absence of meaningful systematic bias in CAMP, which demonstrated a mean count bias of only +1.50 colonies (Figure 2B). The comparator pipelines displayed wide and asymmetrically distributed limits of agreement, confirming that their count errors are not only large in magnitude but also unpredictable in direction (Figure 2C-D).

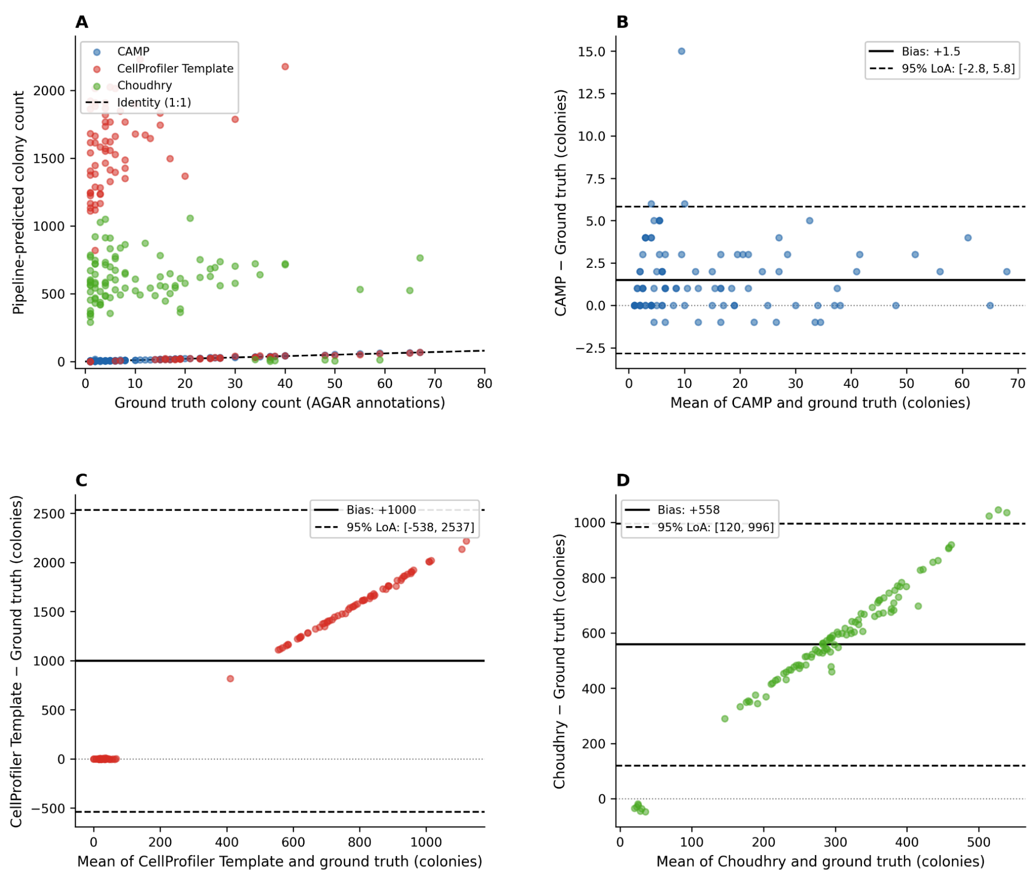

Figure 2. Colony count accuracy across all 100 AGAR benchmark images. (A) Pipeline-predicted counts plotted against ground-truth on a 1:1 identity line. (B-D) Bland-Altman agreement plots for CAMP (B), CellProfiler Template pipeline (C) and Choudhry (D). CAMP shows mean bias of +1.5 colonies; comparators show mean biases exceeding 500 colonies per image.

Colony total area, the sum of all accounted pixels in detected objects in an image by each pipeline, was assessed alongside count accuracy as the other primary biological endpoint to assess performance (Figure 3A-D). The absolute distribution of total detected area per image per pipeline is shown on a logarithmic scale in Figure 3A. Bland-Altman agreement analysis quantifying the systematic bias of each pipeline relative to the ground truth is shown in Figure 3B-D. CAMP produced area estimates closely approximating the ground truth, with a mean bias of -1,268 pixels (SD = 1,422 pixels; 95% limits of agreement: −4,055 to +1,518 pixels). In settings where a control can reach upwards of 120,000 pixels, CAMP's bias is negligible. The CellProfiler Template pipeline and Choudhry pipeline, on the other hand, demonstrated substantially elevated area estimates relative to ground truth, with mean positive biases of +54,098 pixels (SD = 43,682 pixels) and +28,915 pixels (SD = 15,404 pixels), respectively. These magnitudes exceed what would be attributable to proportional scaling error, much like with the colony counts, or consistent with boundary overestimation. Instead, there is a major lack of specificity in the comparators. They consistently misclassify background pixels, including artifacts introduced by agar surface imperfections and condensation, as biological growth. The absolute distribution of total detected area per image, shown on a logarithmic scale in Figure 3A, further supports this: CAMP's area distribution closely reflects the colony annotated distributions, while the CellProfiler Template pipeline and Choudhry distributions are overestimated by approximately one order of magnitude.

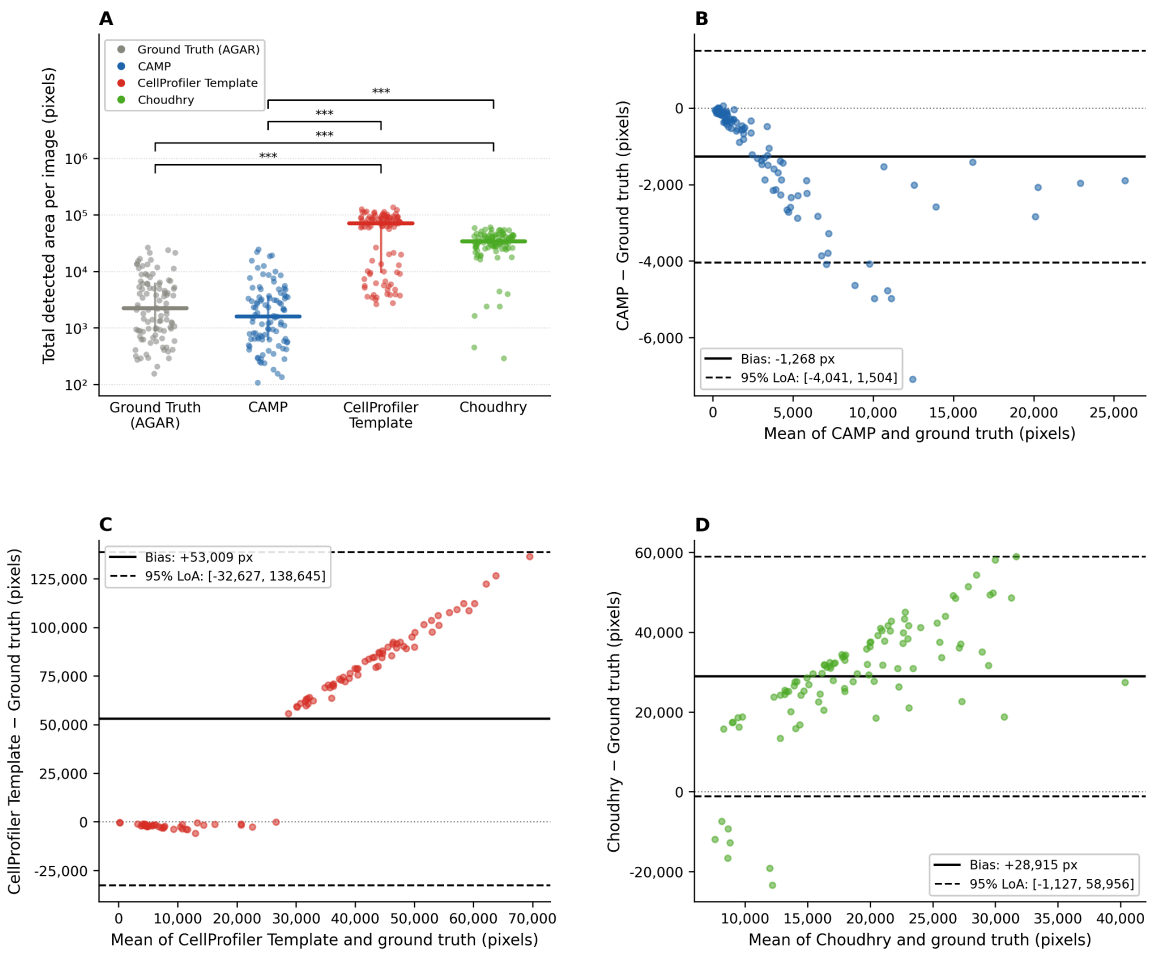

Figure 3. Total Colony area across all 100 AGAR benchmark images. (A) Total detected area per pipeline on a log scale. (B-D) Bland-Altman agreement plots for CAMP (B), CellProfiler Template (C), and Choudhry (D). CAMP shows a mean bias of -1,268 pixels; CellProfiler Template and Choudhry show +54,098 and +28,915 pixels, respectively.

Morphological Feature Consistency

To characterize the biological plausibility of detected objects across pipelines, the geometric properties of each pipeline's output were compared using the panel of four shape descriptors used in the filtering steps of CAMP's workflow (Figure 4). Eccentricity measures how closely an object approximates a perfect circle: a value of zero indicates a geometrically circular object, and values approaching one exhibit more elongated-like shapes. Hence, the lower the eccentricity of an object, the more confident one can be that it represents a discrete, radially symmetric colony rather than an elongated imaging artifact. Solidity measures the proportion of an object's convex hull that is filled by the object itself: values close to one indicate compact, solid masses, while lower values indicate irregular objects with interior voids or concave boundaries, typical of fragmented or jagged detections. Compactness quantifies the relationship between an object's area and its perimeter: a value near one indicates a smooth, efficient boundary as expected of a circular colony, while values well above one indicate long or irregular perimeters relative to their enclosed area, as expected of artifact boundaries rather than smooth colony edges. Lastly, extent measures the fraction of an object's bounding box that is occupied by the object itself: a coherent circular colony fills its bounding box efficiently (approaching $\pi/4$ for a perfect circle), while an irregular object leaves much of its bounding box empty- resulting in significantly lower extent value.

Across all four descriptors, objects identified by CAMP produced values seemingly untainted with noise from the main artifact classes while retaining the full range of biological foreground objects: mean eccentricity of 0.370, solidity of 0.963, compactness of 0.931, and extent of 0.787, whereas the comparator pipelines identified objects whose profiles deviated substantially from biologically plausible values across all metrics. Most notably, the CellProfiler Template pipeline's detected objects exhibited a mean eccentricity of 0.562, substantially higher than CAMP's value of 0.370. This skewed mean eccentricity indicates possible presence of elongated artifacts grouped alongside genuine colonies. The Choudhry pipeline showed the most significant deviation from biologically plausible geometry, with a mean eccentricity of 0.732 and a compactness of 1.269, reflecting susceptibility to irregular, non-disc-like pixel clusters, which the pipeline's limited filtering failed to exclude (Figure 4).

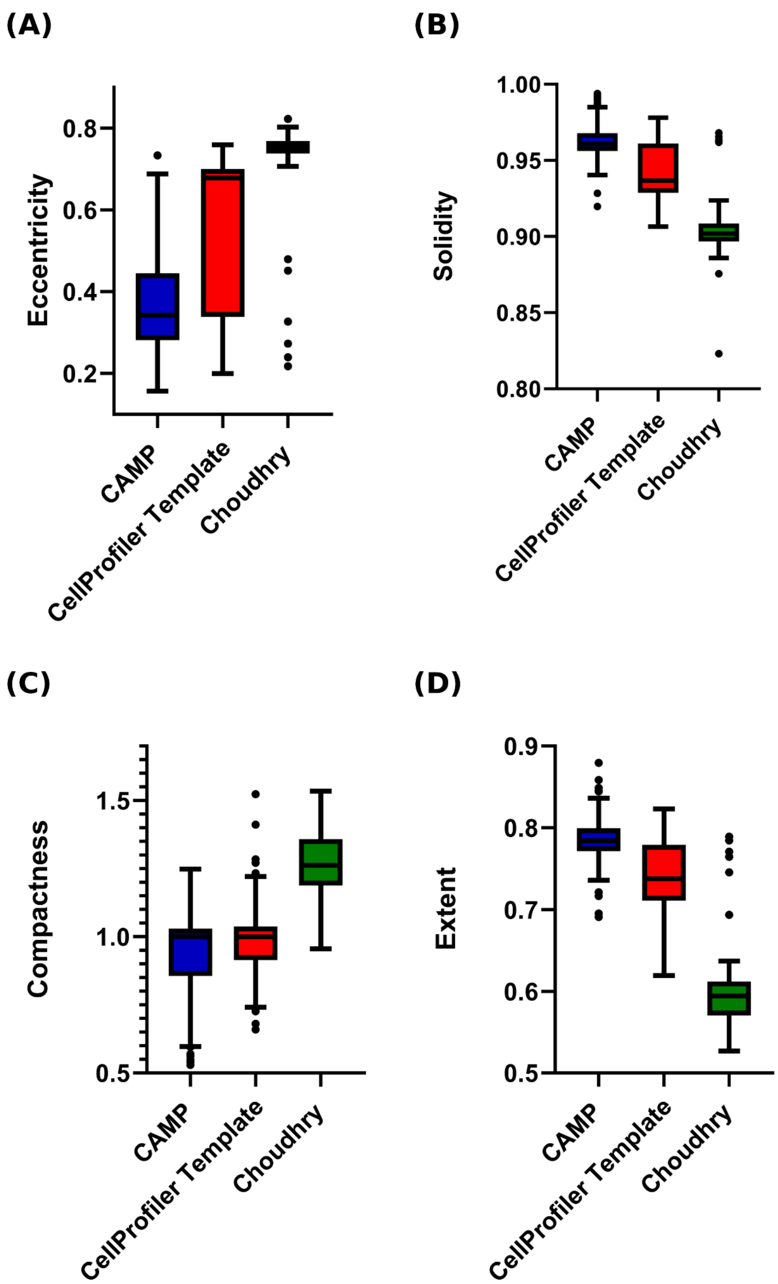

Figure 4. Shape descriptor distributions for detected objects across the 100 AGAR benchmark images. Box plots show per-image mean values of eccentricity (A), solidity (B), compactness (C), and extent (D) for each. CAMP produced the most biologically plausible object profiles across all four metrics.

Pipeline Failure Modes

The density-dependent performance of each pipeline was characterized by plotting per-image F-factor scores against ground truth colony area separately for each pipeline (Figure

5A-C). CAMP shows no relationship between plate density and performance (Figure 5A; Spearman ϱ = −0.030, p = 0.764): data points form a flat, high-valued cloud across the full range of colony areas. The CellProfiler Template pipeline, by contrast, displays a strong bimodal pattern (Figure 5B): data points cluster either near 0.8 or near zero, with a near-complete absence of intermediate F-factor values between 0.10 and 0.50. The failure conditions are confirmed to be density-driven by a strong positive correlation between F-factor and ground-truth colony area (ϱ = 0.922, p < 0.001), meaning the pipeline performs acceptably only on dense plates where genuine colony signal massively outweighs artifact accumulation. The Choudhry pipeline remains near-zero throughout regardless of plate density (ϱ = 0.761, p < 0.001; Figure 5C), confirming that its failure is universal across all imaging conditions rather than caused by specific plate characteristics.

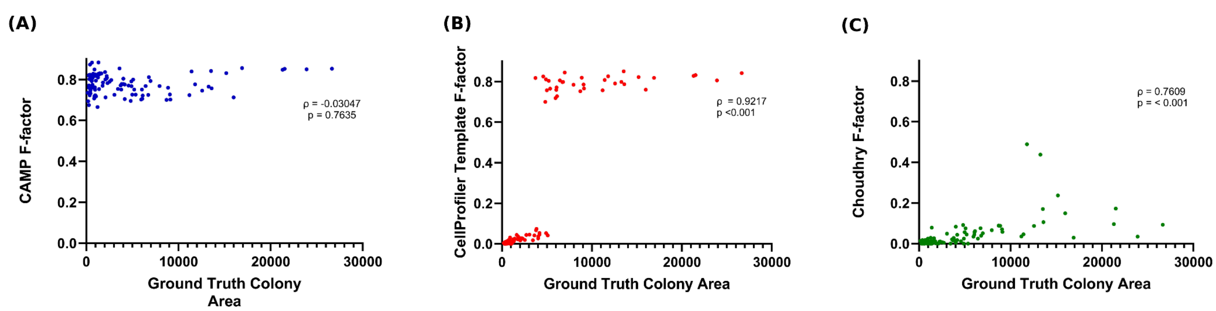

Figure 5. F-factor plotted against ground-truth colony area per image for CAMP (A), CellProfiler Template (B), and Choudhry (C). CAMP shows no density dependence (ϱ = −0.030, p = 0.764); the CellProfiler Template Pipeline exhibits a strong positive correlation confirming density-dependent collapse (ϱ = 0.922, p < 0.001); Choudhry remains near-zero regardless of plate occupancy (ϱ = 0.761, p < 0.001).

The relationship between detected object geometries and identification accuracy was examined by plotting per-image mean shape metrics against per-image F-factor scores for all three pipelines simultaneously (Figure 6). This analysis links the morphological profiles shown in Figure 4 to the performance outcomes reported in Figures 1 and 2, establishing object geometry as a mechanistic indicator of pipeline accuracy rather than an independent observation. Mean eccentricity is the most diagnostically informative predictor for the CellProfiler Template pipeline (Figure 6A): CAMP's data points cluster at low eccentricity and high F-factor, confirming that images where detected objects are compact and radially symmetric correspond to accurate colony identification. The CellProfiler Template pipeline shows a strong and significant negative correlation between mean eccentricity and F-factor ($\varrho = -0.700$, $p < 0.001$), indicating that images where detected objects are more elongated on average correspond directly to worse segmentation performance. The Choudhry pipeline's data points cluster at chronically elevated eccentricity and near-zero F-factor regardless of plate conditions. Since its F-factor scores occupy an extremely narrow range with almost no variance, where 76 of 100 images yield scores below 0.05 and the median is 0.012, formal correlation testing is uninformative for this pipeline, and its failure is, again, better characterized as universal.

Solidity shows a complementary pattern (Figure 6B): higher mean solidity corresponds to higher F-factor. For CAMP no statistically significant relationship between the two is seen ($\varrho = +0.128$, $p = 0.218$), consistent with CAMP consistently detecting well-formed, contiguous colony objects across the full range of solidity values present in the dataset. The CellProfiler Template pipeline exhibits a strong positive correlation ($\varrho = +0.674$, $p < 0.001$), reflecting the fact that images where artifacts drive mean solidity downward are also the images where F-factor collapses. The Choudhry pipeline shows only a marginal positive association ($\varrho = +0.235$, $p = 0.019$), the sole shape metric for which it reaches statistical significance, and its effect size is modest relative to the Template pipeline — consistent with its uniform, density- independent failure. Extent reinforces the Template pipeline's pattern (Figure 6C): CAMP shows no significant association between mean extent and F-factor ($\varrho = -0.074$, $p = 0.476$), while the CellProfiler Template pipeline shows a significant positive correlation ($\varrho = +0.664$, $p < 0.001$), confirming that objects with low bounding-box occupancy are associated with segmentation failure. The Choudhry pipeline shows no significant association for extent (ϱ = +0.113, p = 0.264), consistent with its universally suppressed F-factor distribution.

Compactness shows the least discriminatory pattern across all pipelines. Neither the CellProfiler Template (ϱ = −0.047, p = 0.644) nor the Choudhry pipeline (ϱ = −0.149, p = 0.138) reaches significance for compactness against F-factor, and a marginal association is observed for CAMP (ϱ = +0.205, p = 0.047) that does not survive conservative correction and reflects the inherent variability of this metric at the downsampled image resolution rather than a systematic bias.

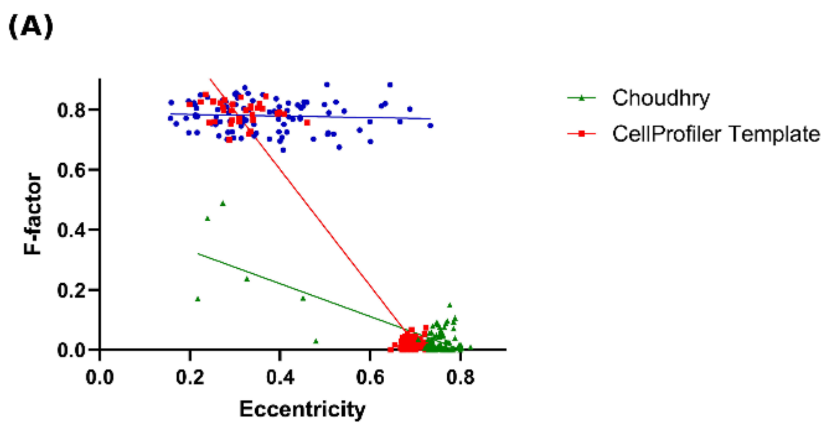

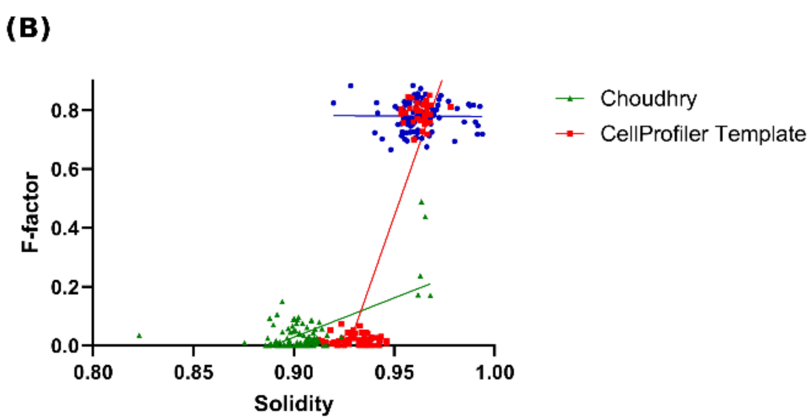

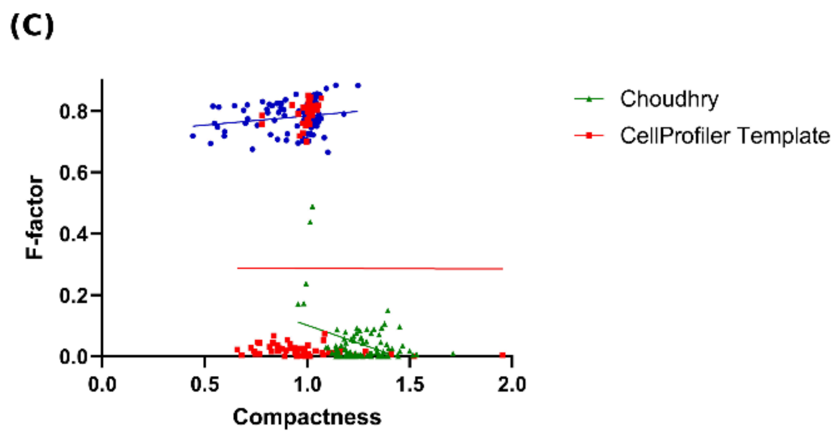

Figure 6. Per-image morphological profiles as correlators of segmentation performance across the 100 AGAR benchmark images. Mean eccentricity (A), solidity (B), and compactness (C) plotted against per-image F-factor, colored by pipeline. CAMP shows no consistent significant relationship between object geometry and F-factor (all $p > 0.05$ under conservative correction). The CellProfiler Template pipeline shows strong significant correlations for eccentricity ($\varrho = -0.700$, $p < 0.001$), solidity ($\varrho = +0.674$, $p < 0.001$), and extent ($\varrho = +0.664$, $p < 0.001$), consistent with its density-dependent failure mode. The Choudhry pipeline shows no significant geometry-dependent variation in F-factor, consistent with its universal failure.

Colony Size Distribution and Morphological Profiles Across Synthetic Overlap Sets

Across all three synthetic overlap sets, the ground-truth colony size distribution exhibited a consistent positively skewed, approximately log-normal profile, with a median of approximately 155–157 pixels and a long right tail extending above 1,000 pixels. This distributional shape is reflective of natural variation in colony size present in the AGAR source images and serves as the reference against which each pipeline's output is evaluated (Figure 7).

At low overlap (Set 1), all three pipelines produced size distributions broadly resembling the control (Figure 7). As overlap increased across Sets 2 and 3, the comparator pipelines diverged substantially from both the control and from their own Set 1 distributions, while CAMP maintained a distribution whose shape closely tracked the control throughout.

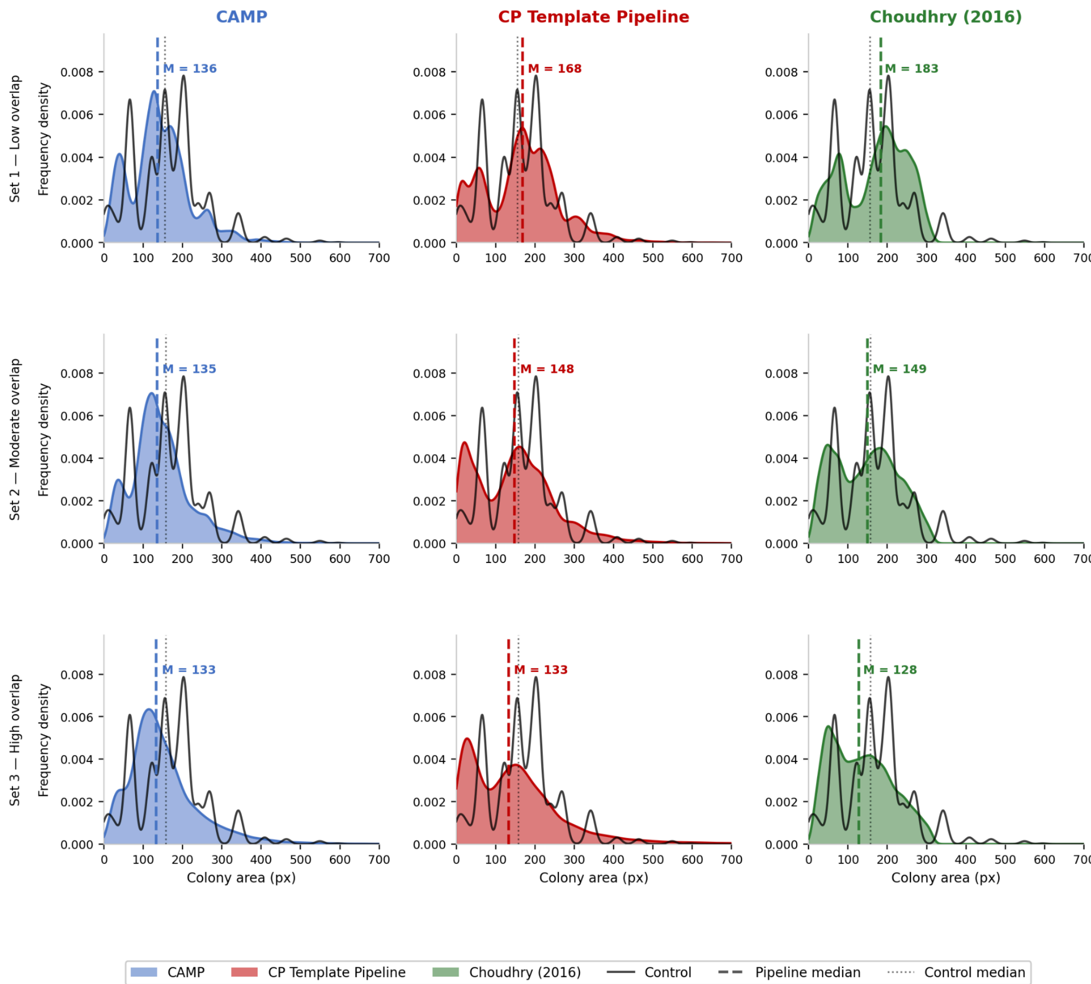

Figure 7. Colony size distributions per pipeline across Set 1 (low), Set 2 (moderate), and Set 3 (high overlap). Ground-truth control distribution overlaid as a solid line per panel. Dashed vertical lines indicate the per-pipeline median, dotted vertical lines indicate control median. Multiple peaks visible in the control curve reflect the discrete colony annotation sizes inherent to the synthetic image construction method.

The most diagnostically informative summary of this divergence is the trajectory of the modal peak location, the colony size at which each pipeline's detected distribution is most concentrated (Figure 8B). The ground-truth control modal peak remained stable at 150 pixels across all three overlap sets. CAMP's modal peak shifted modestly from 130 pixels at Set 1 to 110 at Set 3, a change of −20 pixels. The CellProfiler Template pipeline's modal peak collapsed from 170 px at Set 1 to 10 at Set 2 and 30 pixels at Set 3, a total shift of −140. Choudhry's modal peak fell from 190 at Set 1 to 50, where it remained through Set 3, a total shift of −140. These collapses reflect a near-total redistribution of the detected population away from biologically typical colony size distribution disproportionately toward the lower first quartile threshold. The median detected colony size shows the same trajectory: the control median is stable at 155–157 px across all sets, CAMP shifts by only −3 pixels (136 to 133 pixels), while the CellProfiler Template falls by −35 pixels (168 to 133 pixels) and Choudhry falls by −55 (183 to 128) (Figure 8A).

The zone-based analysis using the interquartile range of the ground-truth control distribution (Q_1 = 107 and Q_3 = 207) directly quantifies the redistribution mechanism. The percentage of detections falling below Q_1, the fragmentation signal, increased by +3.5 percentage points for CAMP across sets (29.6% to 33.1%), compared to +12.3 percentage points for the CellProfiler Template (28.8% to 41.1%) and +12.6 percentage points for Choudhry (28.9% to 41.5%) (Figure 8C). Critically, the control's sub-Q_1 fraction decreased by −2.4 percentage points across the same range, reflecting the expected dominance of larger merged colony masses at higher density. Both comparators therefore move in the opposite direction to the ground truth, confirming that the inflation of sub-Q_1 detections represents a pipeline failure rather than a biological signal. The percentage of detections within the interquartile range, the peak preservation metric, further corroborates this interpretation. The control maintains a stable IQR occupancy of approximately 51.4% across all three sets. CAMP begins above this value at Set 1 (55.4%), reflecting its conservative exclusion of objectively larger objects, and declines to 47.2% by Set 3. The CellProfiler Template maintains IQR occupancy substantially below the control throughout sets, declining from 39.5% to 34.3% (−5.2 percentage points). The Choudhry pipeline faces a different primary phenomenon driving its object size distribution, where its large-object population becomes increasingly fragmented and collapses into the IQR zone. Consequently, its overall distribution shifts leftward and experiences a marginal IQR increase from 34.8% to 39.5% — remaining well below the control reference throughout despite this apparent stabilization.

The mean number of detected objects per image increases across sets for all pipelines, reflecting the greater number of colonies placed at higher overlap conditions (Figure 8E). The ground-truth control rises from 353 to 1019 objects per image from Set 1 to Set 3. All three pipelines fall increasingly short of this count at higher overlap: CAMP detects 703 objects per image at Set 3 (+384 from Set 1), the CellProfiler Template detects 875 (+514), and Choudhry detects 778 (+453). The progressive undercounting relative to the ground truth across all pipelines at Set 3 indicates that there is substantive merging or exclusion of closely adjacent colony masses into single detections or outright missed detections. This net undercounting is most pronounced for CAMP, whose conservative morphological filter excludes geometrically implausible objects, including extreme overlapping masses, rather than accepting them as fragments, reflecting a weakness in its architectural choice that prioritizes specificity over sensitivity under crowding conditions.

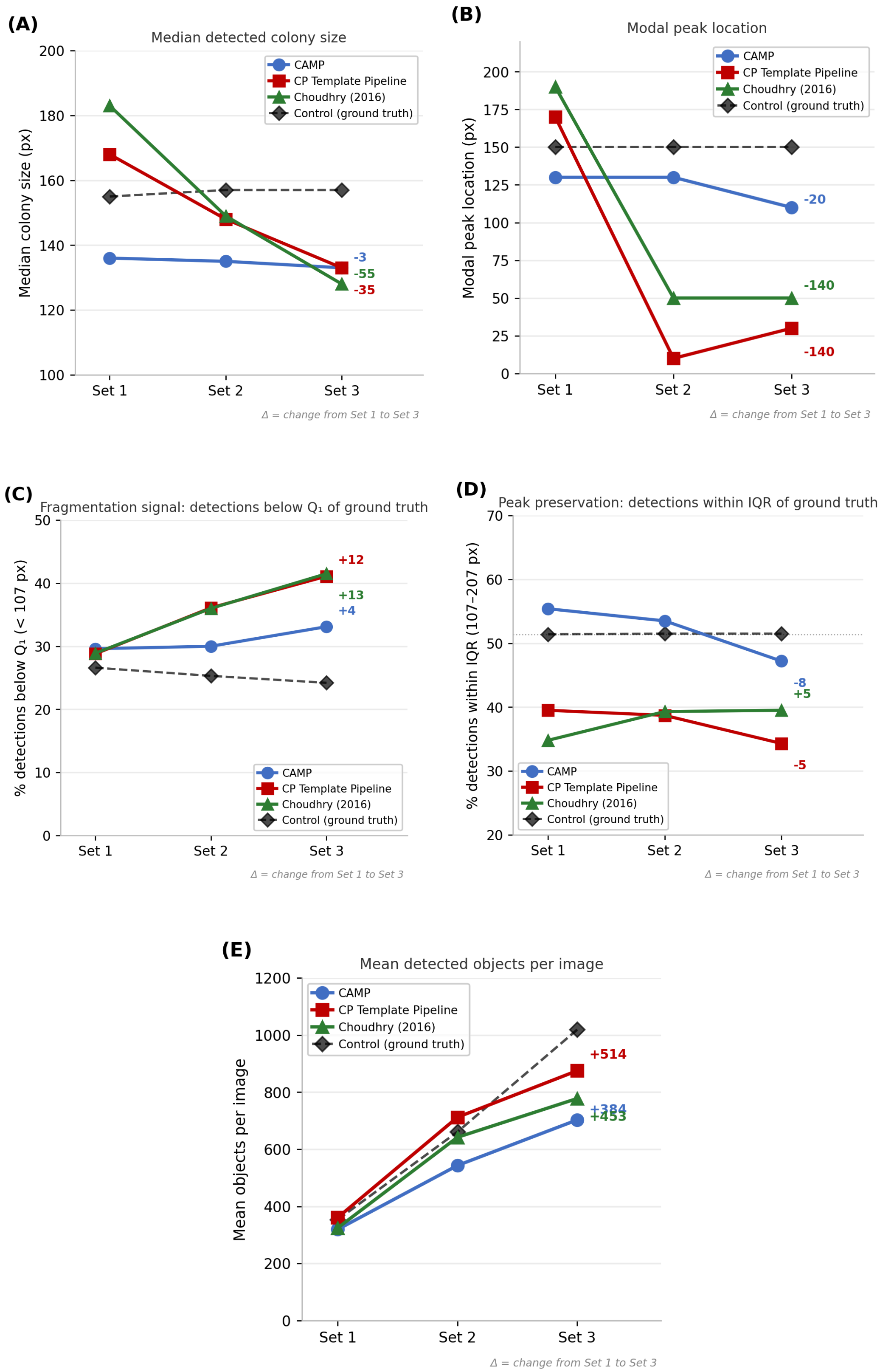
(A)
Median detected colony size
Median colony size (px)
200
180
160
140
120
100
CAMP
CP Template Pipeline
Choudhry (2016)
Control (ground truth)
-3
-55
-35
Set 1
Set 2
Set 3
Δ = change from Set 1 to Set 3
(B)
Modal peak location
Modal peak location (px)
200
175
150
125
100
75
50
25
0
CAMP
CP Template Pipeline
Choudhry (2016)
Control (ground truth)
-20
-140
-140
Set 1
Set 2
Set 3
Δ = change from Set 1 to Set 3
(C)
Fragmentation signal: detections below Q₁ of ground truth
% detections below Q₁ (< 107 px)
50
40
30
20
10
0
+12
+13
+4
CAMP
CP Template Pipeline
Choudhry (2016)
Control (ground truth)
Set 1
Set 2
Set 3
Δ = change from Set 1 to Set 3
(D)
Peak preservation: detections within IQR of ground truth
% detections within IQR (107–207 px)
70
60
50
40
30
20
-8
+5
-5
CAMP
CP Template Pipeline
Choudhry (2016)
Control (ground truth)
Set 1
Set 2
Set 3
Δ = change from Set 1 to Set 3
(E)
Mean detected objects per image
Mean objects per image
1200
1000
800
600
400
200
0
CAMP
CP Template Pipeline
Choudhry (2016)
Control (ground truth)
+514
+384
+453
Set 1
Set 2
Set 3
Δ = change from Set 1 to Set 3

Figure 8. Distributional metrics across synthetic overlap sets for all three pipelines and ground-truth control. Δ values annotated on each panel indicate change from Set 1 to Set 3. (A) Median detected colony size. Δ: CAMP −3 px; CP Template −35 px; Choudhry −55 px. (B) Modal peak location of the detected size distribution. Δ: CAMP −20 px; CP Template −140 px; Choudhry −140 px. (C) Percentage of detections below Q_1 of the ground-truth distribution (< 107 px). Δ: CAMP +4%; CP Template +12%; Choudhry +13%. (D) Percentage of detections within the interquartile range of the ground-truth distribution (107–207 px). Dotted horizontal line indicates the stable control reference value (51.4%). Δ: CAMP −8%; CP Template −5%; Choudhry +5%. (E) Mean number of detected objects per image. Δ: CAMP +384; CP Template +514; Choudhry +453.

To characterize the geometric properties of the objects each pipeline accepts under increasing overlap, the four shape filter criteria were measured across detected object populations at each overlap level. Their trajectories as overlap increases provide a direct readout of each pipeline's segmentation integrity (Figure 9). Across all four metrics, CAMP's detected objects maintain profiles closest to biologically plausible values and exhibit the smallest absolute change across sets. Eccentricity rises by +0.185 from Set 1 to Set 3 for CAMP, compared to +0.323 for the CellProfiler Template and +0.330 for Choudhry. Extent declines by only −0.013 for CAMP, versus −0.145 and −0.157 for the comparators. The pattern across compactness and solidity is consistent across all four descriptors. The objects accepted by the comparator pipelines become progressively more elongated, more irregularly bounded, and less space-filling as overlap increases, a geometric signature consistent with fragmented colony remnants rather than intact colony masses. CAMP's detected objects remain geometrically stable across all three overlap levels, as confirmed by the tight, consistently positioned violin distributions in Figure 9, while the comparator violins broaden and shift substantially with increasing overlap.

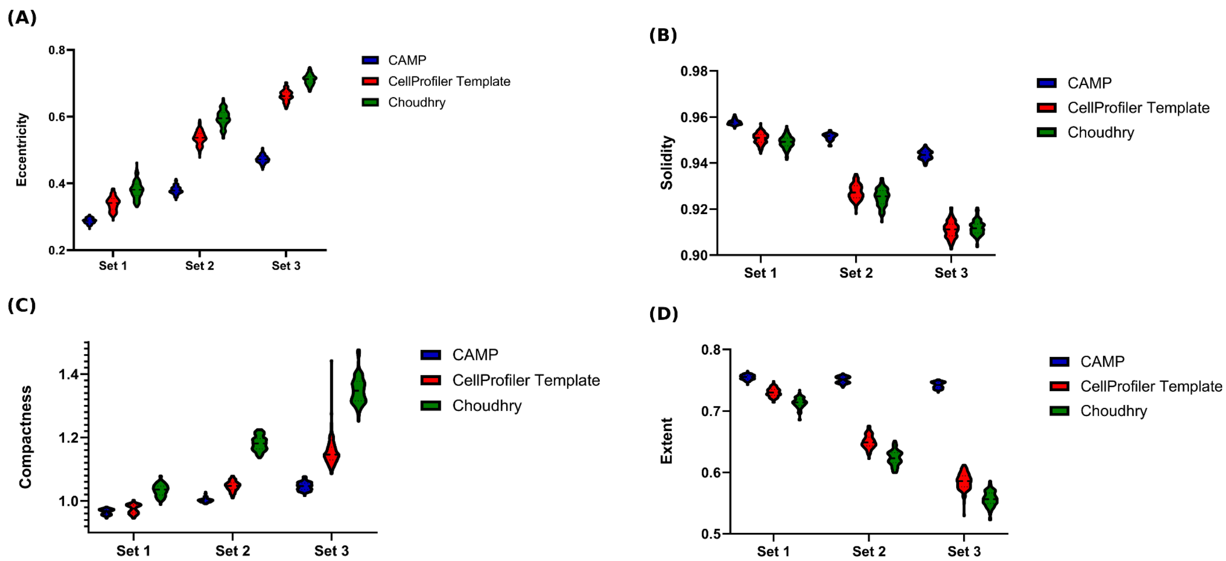

Figure 9. Per-image violin plots of eccentricity (A), solidity (B), compactness (C), and extent (D) for objects detected by each pipeline across synthetic overlap Sets 1–3. Each violin represents the distribution of per-image mean values across the 50 images per species per set. CAMP distributions remain stable across all overlap levels, while comparator distributions broaden and shift toward geometrically implausible values. Δ values indicate the change in mean from Set 1 to Set 3. (A) Mean eccentricity. Δ: CAMP +0.185, CellProfiler Template +0.323, Choudhry +0.330. (B) Mean solidity. (C) Mean compactness. (D) Mean extent. Δ: CAMP −0.013, CellProfiler Template −0.145, Choudhry −0.157.

Discussion

Rationale for Individual Modules

The results confirm that the three failure modes identified in existing pipelines, overreliance on intensity-based thresholding, shape-based declumping of objects calibrated for mammalian cell compartmentalized structures, and the absence of any artifact filtering, are measurable performance deficits. To address the first issue without requiring per-experiment or per-image manual recalibration, CAMP implemented two parallel processing branches that cover the natural range of growth in the image analysis requirements of dense versus sparse plating conditions. In practice, attempts to create a single all-encompassing pipeline repeatedly failed to produce acceptable results when testing across the entire range of colony growth area. In images with abundant growth, the global intensity histogram contains a well-defined foreground peak that a global intensity-based identification algorithm can pick up on. In plates with sparse, attenuated growth, the global intensity histogram lacks such clear divides, and illumination imperfections can take over intensity-based identification due to lack of robust signaling. Global methods under these conditions are likely to miss faint colonies altogether, and mistakenly incorporate substantial noise into the analysis. CAMP's small branch addressed this by substituting an adaptive thresholding strategy that evaluates local pixel regions separately, preserving sensitivity to colonies whose signal is only marginally above local background. In practice, this methodology for primary identification of objects proved efficient in addressing the full range of plating densities and colony morphologies encountered in the study described in Chapter 3, crucially circumventing the need for manual user input in per-experiment or per-image parameter adjustment.

The selection of eccentricity, solidity, compactness, and extent as filter criteria was motivated by the need for shape descriptors that collectively target the main types of noise encountered in the study that are ignorant to properties, such as size, species, growth stage, inherently variant across biological colonies. Eccentricity targets elongated objects such as plastic plate reflections, inoculation stretches, and agar imperfections with eccentricity scores inconsistent with the radial symmetry of colony-forming units. Solidity targets fragmented remnants and objects with interior voids, such as bubbles in the media, whose convex-hull fill fractions fall below the range expected of contiguous colony masses. Compactness targets objects with disproportionately irregular perimeters relative to their areas, such as jagged noise clusters and granular artifacts, while remaining insensitive to size. Extent targets sparse foreground regions with low bounding-box occupancy, discriminating small colonies with plausible form from spotted noise with low bounding-box fitting score. Together, the four criteria form a redundant exclusion filter where one geometric test might fail to exclude an object, but it is bound to be detected and removed by another. Crucially, fixed area thresholds, like the one found in Choudhry, were exclusively avoided to prevent the potential exclusion of genuine colonies from the measurement output [16].

The segmentation logic in CAMP also has substantive methodological deviation from both comparator pipelines. In the comparators, segmentation settings are solemnly shape-based, configured internally within the detection module, and are applied simultaneously to all detected foreground, including artifacts. Any accepted noise contributes to the generation of an object center in segmentation, generating additional regions in already implausible objects, greatly inflating both object count and area. In CAMP, morphological implausible objects are removed, preventing the compounding of errors that occurs when segmentation boundaries are placed within artifact regions. Operating segmentation logic in a modular manner also enables independently configured likely distances between object centers, based on previously built improvements on identification logic, adjusting for dense and sparse growth conditions.

Pipeline Performance, Count and Area Fidelity

The results establish that CAMP achieves substantially superior performances across all evaluated metric categories relative to both comparator pipelines. An important interpretive clarification applies to the F-factor values reported here: the AGAR dataset annotations do not consist of manually traced colony boundaries, but of spatial coordinates from which an ellipse can be computationally extrapolated to approximate colony boundaries [17]. F-factor scores therefore reflect agreement between a pipeline's detected boundaries and an elliptical proxy rather than the exact true colony perimeter. For near-circular colonies the margin of error is minor, but for highly irregular colonies, the elliptical annotation itself deviates from the true boundary, imposing a ceiling on the achievable F-factor score for a given image regardless of identification accuracy. The F-factor scores reported here should therefore be understood as conservative lower bounds on true segmentation performance for all pipelines. The supplemental example image illustrates this directly: CAMP's output with a near 0.79 F-factor score objectively appears to capture colony boundaries more accurately than reported by the F-factor, because the remaining discrepancy is accounted for the annotation ellipses' perimeter mismatch rather than for any missed colonies or inaccurate boundary alignment.

CAMP's precision stands in stark contrast to the varying failure patterns observed in the two comparator pipelines. The CellProfiler Template pipeline shows high inter-image variability in F-factor and ARI (SD = 0.369 and 0.370, respectively), reflecting a bimodal identification behavior in which the pipeline either succeeds or collapses entirely depending on image-specific characteristics such as colony density and illumination. The Choudhry pipeline, by contrast, shows narrow F-factor and ARI variance (SD = 0.075 and 0.072, respectively), because it fails consistently across nearly all images regardless of imaging conditions — 76 of 100 images yield F-factor scores below 0.05, with a median of 0.012. These are mechanistically distinct failure modes: the Template pipeline's performance is condition-dependent, while the Choudhry pipeline's failure is universal.

The ARI distributions reflect this distinction. For the CellProfiler Template pipeline, 64 of 100 images yield ARI values near zero and 11 yield negative values, indicating pixel assignments no better than random chance in those images. This finding is consistent with over-segmentation behavior documented in Figure 4, in which internal colony texturing and uneven illumination are misinterpreted as inter-object boundaries, fragmenting colonies into incoherent detections. For the Choudhry pipeline, 84 of 100 images yield ARI values near zero and 37 yield negative values, indicating random or sub-random pixel assignment across nearly all conditions. This is consistent with the false-positive artifact inclusion documented in Figure 4, where the pipeline's limited morphological filtering accepts irregular, elongated objects alongside genuine colonies, producing object populations whose pixel groupings bear no correspondence to true colony boundaries.

The near-complete absence of over-segmentation artifacts in CAMP, shown through consistent object shape profiles in Figure 4 and high-fidelity colony areas in Figure 3, demonstrates that departing from an all-in-one module structure in favor of individual operators represents a substantive technical improvement. The slight negative area bias of −1,268 pixels (SD = 1,422 px) observed for CAMP warrants brief interpretive consideration, as it is likely a byproduct of the AGAR images' imperfect colony annotations mentioned earlier. However, it is possible that the dual-branch colony identification strategy of CAMP, in the process of focusing on the extreme colony size conditions, is suboptimally identifying certain colonies per image that do not align with the general size trend of the plate — which is a common phenomenon. In practice, CAMP's area estimates are predictable and reliable for comparative biological analyses, as the bias is applied equally across all images within a branch mode.

The low false-positive rates and minimal colony count deviation further confirm that the morphological filter criteria successfully distinguish genuine colony signals from the range of technical artifacts inherent to plate-based imaging, while accepting the full range of biologically plausible foreground objects irrespective of their size, species, or clustering level. The near-zero count bias in CAMP (+1.5 colonies) is particularly important for applicational purposes. In antimicrobial susceptibility screening or functional genomics experiments, where colony counts serve as a direct proxy for growth inhibition or competitive fitness, a systematic bias of this magnitude is unlikely to introduce meaningful confounding data. In the specific case of the study outlined in the following chapter, high count fidelity is crucial for the validation of the VOCs as fungistatic, rather than fungicidal, agents. By contrast, the mean overcounts exceeding 1,000 per image by the CellProfiler Template and approximately 570 for Choudhry render both of less credibility for quantitative applications. The wide and asymmetric limits of agreement for the Template pipeline confirm that these errors cannot be corrected through linear adjustment, as both the magnitude and direction of per-image errors are unpredictable. The Choudhry pipeline's uniformly high counts, despite its near-zero F-factor, reflect the same false-positive artifact inclusion described above: its detections are numerous but have no relationship to actual colony boundaries.

Species Generalizability

A substantive finding of this study is the species-dependent performance observed in the CellProfiler Template pipeline, which recorded an F-factor score approximately 46% lower for *S. aureus* than for *C. albicans*- 0.193 and 0.357, respectively. This disparity is primarily driven by the interaction between colony surface topology and the AGAR dataset's specific imaging conditions. *S. aureus* colonies exhibit a characteristically glossy, convex texture likely to reflect light in a non-uniform manner, creating specular highlights and internal "glare" that exacerbate illumination contrasts. Standard intensity-based pipelines often misinterpret these high-intensity reflections as object boundaries or "holes," leading to the digital shattering of individual colonies into many incoherent fragments.

Furthermore, the color scheme of the AGAR dataset provides a more favorable signal-to-noise ratio for *C. albicans*. The bright white, opaque colonies of *Candida* provide a stark, high-contrast boundary against the darker agar medium, making them clearly discernable. In contrast, the yellow-to-golden hue of *S. aureus* is found much closer in the color spectrum to the low-lit background of the agar plates. This diminished color contrast makes it significantly harder for a global threshold to accurately distinguish colony boundary pixels from background pixels, resulting in higher false-positive and false-negative rates. CAMP, by contrast, demonstrated comparable performances across both organisms by utilizing its dual-branch structure, morphological filters, and adaptive intensity thresholding. These results suggest that CAMP functions as a generalist quantification tool capable of maintaining accurate colony boundary readings across diverse microbial species, whereas the comparator pipelines are functionally constrained to the organism types for which they were originally parameterized.

Morphometric Evidence for Artifact Exclusion

The shape descriptors establish that eccentricity and compactness are the most diagnostically informative indicators of segmentation quality across pipelines: both increase from CAMP to CellProfiler Template to Choudhry, mirroring the F-factor ranking reported in Figure 1. The Choudhry pipeline's mean eccentricity of 0.732 and compactness of 1.269, compared to CAMP's respective 0.370 and 0.931, indicate that its detected objects are substantially more elongated and irregularly shaped than those ultimately reported by CAMP. These are geometric signatures of the different types of noises identified earlier on: plate reflections, condensation, and agar imperfections that the comparator pipelines failed to exclude in their analysis. Their inclusion directly explains the extreme overcounting, area inflation, and near-zero colony boundary fidelity observed. The CellProfiler Template pipeline's intermediate eccentricity (0.562) reflects a partial failure of artifact exclusion consistent with its density-dependent performance: at high density, real colonies consist of the majority of the data, while at low density the absence of shape filtering allows artifacts to accumulate, producing the binary failure mode documented in Figure 5B based on performance against colony area. CAMP's morphometric profile stays rather constant throughout sets and maintains levels expected of real microbial colonies. Beyond artifact inclusion, the geometric profiles of detected objects also serve as reporters of segmentation logic quality more directly: a pipeline that successfully identifies and defines colony boundaries will produce objects more structurally similar to true colonies, while those that struggle to confidently locate and separate colonies in an object will instead produce digital representations, or actively fragment colonies, whose geometry are far removed to the colonies' actual physical characteristics. When segmentation logic shatters foreground signal into arbitrary regions, as occurs when shape-based declumping operates under assumptions fit for cellular compartmentalized structures, the resulting objects are geometrically random, and their eccentricity, solidity, compactness, and extent values stray accordingly from the plausible range that colonies can be found in. The deviation from biologically plausible values by the comparators' analysis is therefore not merely a record of what artifacts tend to be identified, but a reflection of the uncertainty with which these pipelines assumed the desired objects' locations and general features.

Figure 6 examines per-image variation in accepted object geometry and its relationship to per-image segmentation accuracy. Given that all pipelines work with the exact same images and conditions, differences in object geometry can only be attributed to the pipelines' perception of the image and the objects within it. Hence, the correlations reported in Figure 6 characterize how consistently each pipeline's acceptance criteria and segmentation hold across varying images. For the CellProfiler Template pipeline, the strong negative correlation between mean eccentricity and F-factor ($\varrho = -0.700$, $p < 0.001$) reflects the density-dependent pattern established in Figure 5. Solidity and extent show complementary patterns for the same pipeline ($\varrho = +0.674$, $p < 0.001$ and $\varrho = +0.664$, $p < 0.001$ respectively) reinforcing that images where the accepted object pool is approaching geometrically implausible values are also those with poor overall quantification quality. The Choudhry pipeline, by contrast, shows no significant relationship between object geometry and F-factor for eccentricity ($\varrho = -0.153$, $p = 0.129$) or extent ($\varrho = +0.113$, $p = 0.264$), and only a marginal association for solidity ($\varrho = +0.235$, $p = 0.019$). This absence of geometry-dependent structure in its F-factor scores is mechanistically informative: with 76 of 100 images yielding F-factor scores below 0.05 and a median of 0.012, the Choudhry pipeline's failure is effectively universal across all imaging conditions, rendering per-image object geometry an irrelevant variable. Its failure is not conditional on artifact accumulation in specific images, it fails regardless. CAMP, by contrast, shows no consistent relationship between any shape metric and segmentation performance (all $p > 0.05$ under conservative correction), confirming that its identification logic is stable and geometry-independent across the full range of imaging conditions represented in the benchmark dataset.

Synthetic Overlap Validation- Distributional Fidelity and Segmentation Mechanism

The synthetic validation section of this chapter extends benchmarking findings into controlled conditions where inter-colony spatial arrangement is experimentally determined rather than biologically emergent. This approach was designed specifically to determine the degree to which different pipeline architectures deteriorate as a function of spatial crowding, a confound expected to occur with microscopy-biased algorithms applied in a petri dish context. By isolating overlap as the primary variable, the study provides a stringent test of whether CAMP's performance advantage is grounded in its architectural logic or is merely a byproduct of the specific characteristics of the real-image benchmark dataset.

A critical interpretive note before examining the results concerns the nature of synthetic image data. Although drawing colony patches from the subset of the 100 original AGAR images and recompositing them at controlled area overlap retains biological authenticity in individual colony morphology, it necessarily simplifies several properties of organically grown petri dishes. Color gradients between adjacent colonies, surface tension effects at colony boundaries, differential growth rates, and the optical complexity of genuine colony-on-agar interfaces are not fully reproduced in the synthetic construction. The results of this validation should therefore be understood as characterizing pipeline behavior under controlled and interpretable, yet inflated, spatial conditions rather than as a direct simulation of all real-world imaging scenarios.

The primary finding of the synthetic validation is that both comparator pipelines fail through a common mechanism as overlap increases: the progressive redistribution of detected colony mass away from the biologically normal size range, with touching colony masses fragmented into fractional distorted objects of true colonies that inflate the small-object zone while simultaneously, at low to moderate overlap, a disproportionate representation of large merged objects inflates the large-object zone. In tandem, the shifts towards the small and large object size extremes produce a hollowing out of the central peak that drives the detected size distribution away from ground truth, while surprisingly cancelling out erroneous measures of colony count from one another. This conclusion is supported by convergent evidence across multiple metrics. The modal peak location, the most sensitive indicator of where the bulk of the distribution is concentrated, crashes from 170 pixels and 190 pixels at Set 1 for the CellProfiler Template and Choudhry respectively, to 10–30 and 50 by Set 3, while the control peak holds stable at 150 pixels across all sets and CAMP's peak shifts modestly from 130 to 110 px. The median follows the same trajectory: the CellProfiler Template falls by −35 pixels and Choudhry by −55 pixels from Set 1 to Set 3, compared to −3 for CAMP and a stable +2 for the control. The zone analysis using the control interquartile range (Q_1 = 107 pixels, Q_3 = 207 pixels) confirms that this distributional collapse is driven by inflation of the sub-Q_1 fraction: both comparators accumulate approximately +12 percentage points more detections below Q_1 by Set 3, moving in the opposite direction to the control, which correctly loses small-object detections as larger merged colony masses dominate at higher density.

The geometric properties of the detected objects provide the mechanistic explanation for these distributional findings. Both comparators' detected objects become progressively more elongated, irregularly bounded, and spatially inefficient as overlap increases, across all four shape descriptors simultaneously. This geometric trajectory is consistent with a mixed population of detected objects: colony masses fragmented into irregular remnants, which produce high eccentricity and low extent, and composite merged masses whose irregular boundaries produce elevated compactness and reduced solidity. The relative contribution of each process differs between the two pipelines and across overlap levels, as discussed above, but both drive detected object geometry away from the compact, radially symmetric profile expected of an intact colony. CAMP's detected objects maintain geometrically stable profiles across all three overlap levels, as shown in Figure 10, reflecting the effectiveness of its identification logic as well as its morphological filter in excluding the most geometrically implausible detections, whether fragments or oversized composites, while accepting objects whose geometry remains consistent with biologically plausible colony morphology.

The two comparator pipelines arrive at this shared outcome through different architectural pathways, and the trajectory of the large-object zone (above Q_3) across sets is particularly informative about how each failure mode unfolds. At Set 1, both comparators over-represent large objects relative to the ground truth: the CellProfiler Template reports 31.7% of detections above Q_3 and Choudhry reports 36.3%, compared to the control's 22.0%. This elevation at low overlap reflects a tendency in both pipelines to merge adjacent but non-overlapping colonies into single oversized detections, a failure mode that precedes and compounds the fragmentation that dominates at higher overlap. As crowding increases, this inflated large-object population collapses: the CellProfiler Template's above-Q_3 fraction falls to 24.6% by Set 3 and Choudhry's falls to 19.1%, both converging toward or below the control's 24.3%. The mass that leaves the large-object zone does not redistribute correctly into the IQR, where the control remains stable at approximately 51%, but instead accumulates in the sub-Q_1 fragment zone, which rises by +12 percentage points for both comparators simultaneously. The net result is a double distortion: an initial overrepresentation of large objects that gives way to an overrepresentation of small ones, with the normal colony size range depleted throughout.

The architectural mechanisms underlying these trajectories differ between the two pipelines. The CellProfiler Template's shape-based declumping logic, calibrated for the well-separated compartments of mammalian cells, first merges spatially adjacent colonies into composite masses at low overlap and then, as overlap increases further and intensity gradients become too shallow to resolve boundaries reliably, subdivides those composite masses into multiple smaller fragments. The pipeline is therefore susceptible to both failure modes in sequence, with the transition between them occurring somewhere between Set 1 and Set 2. The Choudhry pipeline's rigid size ceiling operates differently: it suppresses large-object formation from the outset by imposing a hard upper limit on detectable object size, which explains why its above-Q_3 inflation at Set 1 is driven not by genuine large-object detection but by objects that narrowly exceed the ceiling threshold and are therefore partially reported. As crowding increases and composite masses form, the ceiling forces them into fragmented sub-detections rather than allowing them to be reported. In both cases the distributional consequence across all three overlap levels is equivalent: the IQR zone is chronically under-occupied, the sub-Q_1 zone inflates progressively, and the large-object zone collapses from an initially inflated baseline.

CAMP is not without its own limitations under high-overlap conditions. Its conservative morphological filter, while effective at excluding fragmented and artifact objects, also results in a consistent downward bias in median colony size estimates relative to the ground truth, a systematic offset of approximately −21 px on average across all three sets. This offset reflects the exclusion of borderline large objects whose geometry becomes ambiguous under crowding, rather than a random or unpredictable error. Additionally, CAMP increasingly undercounts detected objects at Set 3 relative to the ground truth control, indicating that closely adjacent colony clusters are merged or excluded rather than individually resolved. These properties are characteristic of a pipeline that prioritizes specificity over sensitivity: it accepts fewer objects overall and accepts them conservatively, but the objects it does accept are geometrically consistent with real colonies and their distributional shape closely tracks the ground truth.

These specific limitations directly inform the analytical design of Chapter 3. Because CAMP's conservative behavior affects individual object size estimates most strongly under conditions of high colony density, precisely the conditions that characterize uninhibited control plates, per-object mean area measurements would carry a density-dependent bias between experimental conditions. Total detected colony area, by contrast, is robust to whether borderline overlapping colonies are segmented as one object or two, as the foreground pixels are counted either way. The adoption of total colony area as the primary dependent variable in Chapter 3 therefore addresses the residual segmentation imprecision that persists even with CAMP's improvements over existing alternatives, ensuring that the biological comparisons reported are not confounded by density-driven measurement artifacts.

Chapter 3: The CviIR Quorum Sensing System Regulates Volatile-Mediated Antifungal Activity in Chromobacterium vaccinii BUC-1

Introduction

The genus Chromobacterium comprises a group of Gram-negative, facultatively anaerobic, motile rods found predominantly in soil and water environments across tropical and subtropical regions [19–23]. Members of this genus are characterized by the production of the violet pigment violacein, a bisindole compound synthesized from two molecules of L-tryptophan via a five-enzyme pathway encoded by the vioABCDE operon [24–28]. Violacein production has been most thoroughly characterized in *Chromobacterium violaceum*, the type species of the genus, which has served as the primary model organism for studying chromobacterial biology, quorum sensing, and secondary metabolite production [19,22,29,30]. Furthermore, *C. violaceum* is the most extensively studied species within the genus, in part owing to its clinical relevance as a human pathogen capable of causing severe systemic infections, and has been the subject of comprehensive pharmacological and industrial reviews [29].

Members of the *Chromobacterium* genus employ a diverse and overlapping array of competitive strategies in the polymicrobial soil and water environments they inhabit. Violacein itself functions not only as a pigment but as a potent broad-spectrum antibiotic: purified violacein from *C. violaceum* has been demonstrated to exhibit bactericidal activity against Gram-positive pathogens including *Staphylococcus aureus*, methicillin-resistant *S. aureus* (MRSA), and *Staphylococcus epidermidis*, disrupting membrane function through mechanisms that differ from conventional antibiotics and that are effective against both planktonic and biofilm-associated cells, with synergistic effects also observed in combination with commercially available antibiotics [31,32]. Beyond this diffusible antibiotic activity, members of the genus also deploy a quorum sensing-regulated Type VI Secretion System (T6SS) as a contact-dependent competitive mechanism: the T6SS injects toxic effector proteins directly into adjacent bacterial cells via a contractile nanomachine that requires multiple non-redundant VgrG tip proteins for full competitive activity, providing a means of suppressing bacterial competitors through direct cell-to-cell assault [33]. Together with the volatile-mediated inhibitory activity against fungal competitors described below, these capabilities position *Chromobacterium* as an ecologically versatile competitor capable of suppressing both bacterial and fungal rivals through parallel and mechanistically distinct strategies.

A more recently characterized species, *Chromobacterium vaccinii*, was originally isolated from native and cultivated cranberry bogs and irrigation ponds and shares many phenotypic characteristics with *C. violaceum*, including violacein production and the possession of a functional N-acyl homoserine lactone (AHL)-based quorum sensing system [20,23,34]. Quorum sensing (QS) is a cell-density-dependent regulatory mechanism by which bacteria coordinate gene expression in response to the extracellular accumulation of diffusible signaling molecules called autoinducers. In *Chromobacterium* species, this system is organized around the CviIR two-component circuit: CviI is an AHL synthase responsible for synthesizing the cognate autoinducer N-hexanoyl-L-homoserine lactone (C6-HSL), while CviR is the cognate LuxR-type transcriptional regulator that binds C6-HSL and subsequently activates or represses target gene expression through a well-characterized DNA-binding mechanism [25,32,35,36]. The CviIR system has been shown to regulate violacein biosynthesis, biofilm formation, and a range of other secondary metabolic processes in a cell-density-dependent manner.

A critical complexity in the CviIR regulatory landscape, one directly relevant to the interpretation of the present work, concerns the scope and composition of the CviR regulon. The established model of AHL-dependent quorum sensing describes a canonical, autoinducer-dependent regulon in which CviR activity requires prior binding of C6-HSL: autoinducer accumulates extracellularly as cell density rises and, once a threshold concentration is reached, binds CviR to enable transcriptional regulation of downstream target genes. However, evidence has emerged indicating the existence of a CviI-independent regulon in which CviR can modulate gene expression even in the complete absence of its cognate autoinducer, demonstrating that this receptor is capable of acting as a broader transcriptional regulator through mechanisms that do not require AHL binding [32]. Critically, the complete global regulon of the CviIR system, the full complement of genes subject to CviR-dependent regulation through canonical autoinducer-dependent and CviI-independent pathways combined, remains undefined in the current literature [32,37–39]. This incompleteness has direct bearing on any experiment that manipulates CviR activity, since the target gene set affected by such perturbations has not yet been comprehensively characterized.

Beyond the well-studied contact-mediated and diffusible antimicrobial activities of violacein, members of the Chromobacterium genus have recently been observed to suppress fungal growth through a distinct volatile-mediated mechanism that does not require direct contact between the bacterium and the fungal target [7,34]. Volatile organic compounds (VOCs) emitted by bacteria represent a chemically diverse class of low-molecular-weight metabolites capable of diffusing through the gas phase and mediating long-range microbial interactions. In this study, bacterial and fungal cultures are physically separated but share a common, controlled environment, such that only gas-phase compounds are shared between them [7]. Under these conditions, *C. vaccinii* BUC-1, the laboratory-isolated strain used throughout this work, reproducibly and significantly inhibits the growth of *Candida albicans* and a range of other clinically relevant fungal pathogens (Montaquila et al., manuscript in preparation), and induces a novel volatile metabolite profile in response [4]. Preliminary characterization of this inhibitory activity's effective range of fungal species following the compiled priority pathogens list issued by the World Health Organization has demonstrated that

BUC-1 volatile emissions suppress the growth of all tested species [4]. *Candida albicans* was selected as the primary model organism for mechanistic investigation in the present work owing to its clinical prominence: it is the most common causative agent of invasive candidiasis, responsible for the majority of hospital-acquired fungal infections worldwide [5], and it is present in the top 4 highest-priority species on the WHO fungal priority pathogen list for the development of novel antifungal interventions.

Given the established literature demonstrating direct antifungal and antibacterial activity of violacein from related *Chromobacterium* species, an initial and necessary question is whether the volatile-mediated inhibitory activity observed here is attributable to the volatilization or vapor-phase activity of violacein itself, or to a distinct class of VOCs regulated independently. This question is addressed in the first experimental section of this chapter through two complementary approaches: characterization of a spontaneous pigment-null variant of *Chromobacterium subtsugae* ATCC 31532, a strain reclassified from *Chromobacterium violaceum* ATCC 12472 and its quorum biosensor mutant CV026, and mutagenic disruption of the *vioE* gene encoding the terminal enzyme in the violacein biosynthesis pathway in BUC-1 [40]. Having established the violacein-independence of the volatile inhibitory activity, the second experimental focus of this chapter is the CviIR quorum sensing system. A chromosomal insertion mutant of the *cvi*R gene in BUC-1 was constructed and characterized, and its volatile inhibitory activity against *C. albicans* was evaluated alongside the wild-type strain. The results demonstrate a direct and significant dependence of the antifungal VOC phenotype on a functional CviR receptor. Chemical validation of this conclusion is provided through quorum-quenching compound experiments, and the inability of exogenously supplied AHL to rescue the cviR mutant phenotype is documented as confirmation that the mutant is functionally deaf to quorum sensing input — the non-viable receptor renders the cell unable to generate the autoinducer signal, meaning both the canonical autoinducer-dependent and CviI-independent CviR regulons are constitutively silenced regardless of extracellular AHL concentration.

Materials and Methods

Microbial Strains, Culture Conditions and Imaging Processing

Chromobacterium vaccinii BUC-1 is the primary bacterial strain used throughout this work and was maintained on King's Medium B (KMB) agar at 30°C. The BUC-1 strain was isolated by a member of the Nau laboratory in water and soil samples from Rhode Island (Montaquila et al., manuscript in preparation). The BUC-1 *cvi*R mutant (Δ*cvi*R::Km^r) and the BUC-1 *vioE* insertion mutant (Δ*vioE*::Km^r) were constructed by insertion mutagenesis described below. For all experiments involving the mutant strains, they were continuously grown on KMB agar supplemented with kanamycin (50 µg/mL) and ampicillin (100 µg/mL) at 30°C to maintain chromosomal selection pressure. *Chromobacterium subtsugae* ATCC 31532 and its spontaneous pigment-null variant were maintained on KMB agar at 30°C. *Candida albicans* SC5314, provided by Eleffherios Mylonakis, MD, PhD, was used as the primary fungal model organism and was maintained on Sabouraud Dextrose Agar (SDA) at 30°C. All strains were stored at −80°C in 20% glycerol stocks for long-term preservation.

Images were acquired in a darkened room using a downward-directed ring light over a dark non-reflective background surface, minimizing ambient light interference and producing consistent illumination across the plate surface. All other image preprocessing steps follow the materials and methods section from the previous Chapter, outlining the cropping, and CellProfiler preprocessing steps before image analysis through CAMP.

Construction of Chromosomal Insertion Mutants

Synthetic DNA fragments containing homologous regions for targeted gene disruption were designed in the Nau lab and synthesized by Twist Bioscience. For the *vioE* mutant, a ~350 bp fragment of the *vioE* gene was synthesized and designated as the homologous recombination target, while a ~275-300 bp fragment was prepared for the *cvi*R mutant.

To generate the mutants, each fragment was synthesized into pTwist Kan High, a non-replicating, suicide vector in BUC-1. The vector carries a kanamycin resistance cassette but lacks an origin of replication functional in *Chromobacterium vaccinii*, enforcing its integration in the target host. The resulting constructs were designated TwistKanHi_vioE_dis_v3 (for *vioE* disruption) and TwistKanHi_Cvacc_cviR-d (for *cvi*R disruption).

The plasmids were first transformed into a mobilizable donor *E.coli* strain for propagation. Targeted gene disruption in *C. vaccinii* was subsequently achieved via bacterial conjugation (mating). Donor *E.coli* and recipient BUC-1 cells were grown to mid-log phase, harvested, and mixed in non-selective agar to facilitate cell-to-cell contact and plasmid transfer. Because the vector cannot replicate autonomously in *C. vaccinii*, kanamycin-resistant transformants could only arise through chromosomal integration of the plasmid via homologous recombination at the targeted loci.

Exconjugants were selected on KMB agar supplemented with both kanamycin (50 μg/mL) and ampicillin (100 μg/mL). Ampicillin selection served to exclude residual donor *E. coli*, as the BUC-1 strain is naturally resistant to this antibiotic. For the *cvi*R mutant, disruption was confirmed by PCR amplification of the insertion sites using plasmid-specific primers in tandem with chromosomal primers flanking the *cvi*R gene. For the *vioE* mutant, disruption was confirmed phenotypically by the complete loss of purple violacein pigment, as the gene is critical for the violacein biosynthetic pathway.

Volatile Organic Compound Inhibition Assay

All volatile inhibition experiments used a sandwich plate format in which bacterial and fungal cultures in individual petri dishes were co-incubated while taped together, forming a seal, without any direct contact or media connectivity, following the assay format established by precedent work in the field [7,34]. Bacterial strains were pre-cultured on KMB agar, then harvested and adjusted to OD_{600} = 2.0; 100 µL of this suspension was used to inoculate fresh KMB bottom plates, which were incubated at 30°C for 48 hours. Mutant strains were cultured on KMB supplemented with kanamycin (50 µg/mL) and ampicillin (100 µg/mL). *C. albicans* SC5314 was prepared from an OD_{600} = 2.0 suspension diluted 10^{-4} and inoculated (100 µL) onto SDA top plates immediately before sandwich assembly. Plates were sealed with laboratory tape and co-incubated at 30°C for 48 hours, after which *C. albicans* growth was quantified using CAMP. All experiments used a minimum of three biological replicates per condition.

Chemical Disruption and Modulation Experiments

2,3-Dimethoxycinnamic acid (2,3-DMCA; Thermo Scientific Chemicals; MW 208.21 g/mol; purity ≥98%; CAS 4046-02-0) was prepared as a 100 mM stock solution by dissolving 500 mg of powder in 24.0 mL of DMSO, vortexed until clear, and stored in foil-wrapped 50 mL Falcon tubes at −20°C. The target working concentration for violacein suppression experiments was 3,230 µM (equivalent to 672 µg/mL), achieved by adding 100 µL of the 100 mM stock to 3 mL of King's Medium B (KMB) broth per well. This concentration was selected to achieve near-complete suppression of CviR-regulated violacein production, building on the 73.9% suppression reported at 150 µg/mL in *C. violaceum*, while staying within reasonable bounds underscored by the original study's MIC of 2,3-DMCA [41]. The mechanistic basis of 2,3-DMCA as a competitive antagonist of the CviR autoinducer-binding domain is described in the Discussion.

Experiments were conducted in six-well cell culture plates housed in sealed anaerobic gas-pack containers (Thermo Scientific AnaeroPack-Anaero). Three conditions were established in parallel: (1) BUC-1 in KMB without 2,3-DMCA (bacteria-only control), (2) BUC-1 in KMB with 2,3-DMCA at 3,230 μM (experimental), and (3) KMB with 2,3-DMCA but no bacteria (chemical-only control). Each condition occupied three wells of a six-well plate, with approximately 3 mL of KMB per well. *C. vaccinii* BUC-1 was grown overnight in KMB broth at room temperature, then normalized the following day to OD_{600} = 0.7 and diluted 10^{-4} in the final well volume. Six-well plates were incubated at room temperature on an orbital shaker at medium speed inside the sealed gas-pack boxes. After overnight bacterial incubation, *C. albicans* SC5314 was standardized to OD_{600} = 2.0, diluted 10^{-4}, and 100 μL was used to inoculate one SDA plate per box. SDA plates were placed inside the sealed boxes and co-incubated with the bacterial cultures at 30°C for 48 hours, after which *C. albicans* colony growth was imaged and quantified using CAMP.

Violacein production was quantified by ethanol extraction. Prior to sampling, 100 μL of each well culture was mixed with 0.9 mL of water in a cuvette and OD_{600} was measured (1:10 dilution) to enable subsequent per-cell normalization. A 300 μL aliquot of each well culture was transferred to a 1.5 mL microcentrifuge tube and centrifuged at 14,000 × g for 20 minutes at room temperature. The supernatant was discarded and the pellet was resuspended in 1.0 mL of ethanol and vortexed vigorously until the pigment was fully dissolved. Tubes were centrifuged at 12,000 × g for 10 minutes to pellet cell debris, and the clarified violet supernatant was transferred to a fresh tube before measuring absorbance at 575 nm (OD_{575}) on a plate reader. Normalized violacein production was expressed as a ratio of absorbance as: OD_{575}/OD_{600}. Three independent biological runs were performed, each with three replicate wells per condition (n = 9 wells total per condition across all runs).

N-Acyl Homoserine Lactone Supplementation

To test whether exogenous autoinducer could rescue the inhibitory phenotype of the Δ*cvi*R mutant, N-hexanoyl-L-homoserine lactone (C6-HSL; CAS 147852-83-3; Cat. No. BBF-04581; MW 199.25 g/mol; $C_{10}H_{17}NO_3$; purity 95%) was dissolved in DMSO and incorporated into molten KMB agar cooled to approximately 45°C, yielding a final concentration of 10 µM throughout the agar. Control plates received an equivalent volume of DMSO without C6-HSL. Bacterial inoculation and sandwich plate assembly followed the standard volatile assay protocol. Agar-incorporated AHL was used rather than suspension-added AHL to ensure continuous autoinducer availability throughout the full 48-hour bacterial incubation period [25].

Statistical Analysis

All colony count data were exported from CAMP as described in Chapter 2. Growth area measurements served as the primary quantitative endpoint for all volatile inhibition experiments, with colony count data reported as a supplementary readout. Statistical comparisons between two conditions were performed using independent samples t-tests (two-tailed). Where three or more conditions were compared, pairwise comparisons were conducted with Bonferroni correction for multiple testing. Mann–Whitney U tests were applied as non-parametric verification for key comparisons and One-Way Anova tests for parametric comparisons. All analyses were performed in

GraphPad Prism (version 3.10.0). Results are expressed as mean ± standard deviation unless otherwise stated. Significance thresholds are $p < 0.05$ (*), $p < 0.01$ (**), and $p < 0.001$ (***).

Results

The following sections present the results of four experimental lines of investigation, each addressing a distinct facet of the molecular regulation of volatile-mediated antifungal activity in *C. vaccinii* BUC-1. The first two sections establish that the inhibitory activity is independent of violacein using both a natural pigment-null variant and a targeted *vioE* mutant. The third section demonstrates that *cvi*R is required for full inhibitory activity. The fourth section examines the effect of AHL supplementation on the *cvi*R mutant phenotype. The last explores the extent of chemical disruption of quorum-sensing in the model organism and what it is observable about the regulation of VOCs via its results.

.

Chromobacterium subtsugae Pigment-Null Variant Retains Full Volatile Inhibitory Activity

To begin assessing whether violacein contributes to the volatile-mediated antifungal activity observed in *Chromobacterium* species, a spontaneous pigment-null variant of *Chromobacterium subtsugae* ATCC 31532 was characterized. This variant, which arose spontaneously during routine culture and was confirmed to lack detectable violacein production by visual inspection, provides a naturally occurring system in which violacein production halts without genetic manipulation of the primary strain under study. If violacein were the principal or sole active VOC responsible for fungal inhibition, the pigment-null variant would be expected to show a substantially reduced inhibitory phenotype relative to the pigment-producing parent strain.

Volatile exposure assays comparing *C. subtsugae* ATCC 31532 and its pigment-null variant against *C. albicans* SC5314 revealed no significant difference in inhibitory activity between the two strains (Figure 10A). Both the pigment-producing parent and the pigment-null variant produced equivalent and substantial reductions in *C. albicans* growth area relative to the no-bacteria control condition. Quantification by CAMP confirmed that *C. albicans* growth area in the presence of the pigment-null variant was reduced by 80.9% relative to control (mean ± SD: 19,203 ± 8,143 vs. 100,525 ± 12,632 pixels), compared to 84.5% reduction in the presence of the pigment-producing parent (15,583 ± 7,428 pixels)- showing no statistically significant difference between one another ($p > 0.05$). The difference between fungal colony counts exposed to the two strains was not statistically significant ($p = 0.44$, independent samples t-test; Figure 10B).

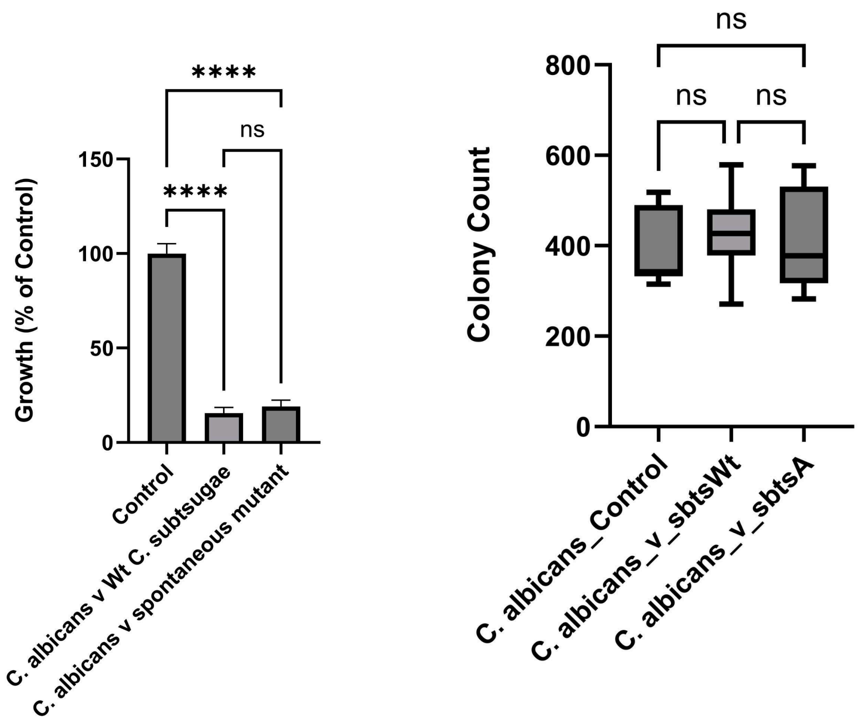

Figure 10. ***C. albicans*** **growth and colony counts following volatile exposure to** ***C. subtsugae*** **ATCC 31532 and its spontaneous pigment-null variant. (A)** ***C. albicans*** **SC5314 growth area expressed as a percentage of the no-bacteria control following 48 hours of volatile co-incubation at 30°C. Both the pigment-producing parent and the pigment-null variant significantly reduced fungal growth relative to control ($p < 0.001$ for both); no significant difference was observed between the two bacterial strains (ns). (B)** ***C. albicans*** **colony counts following volatile exposure to** ***C. subtsugae*** **ATCC 31532 (pigmented) and its pigment-null variant. No significant difference between strains ($p = 0.44$); both produced significantly reduced colony counts relative to the no-bacteria control ($p < 0.001$ for both).**

Disruption of *vioE* in BUC-1 Does Not Attenuate Volatile Inhibitory Activity

To corroborate the *C. subtsugae* result within the primary strain under study, a targeted insertion mutant of the *vioE* gene was constructed in BUC-1. The *vioE* gene encodes the final enzyme in the violacein biosynthesis pathway and is required for the terminal cyclization step that produces the mature violet pigment; its disruption results in complete abolition of violacein production while leaving upstream pathway intermediates intact. Loss of pigmentation in the BUC-1 Δ*vioE* mutant was confirmed visually and by the absence of characteristic violet coloration in liquid culture. The Δ*vioE* mutant is otherwise phenotypically indistinguishable from wild-type BUC-1 in terms of growth rate, colony morphology, and motility, indicating that the insertion did not impose a general fitness cost.

Volatile exposure assays comparing BUC-1 wild-type and BUC-1 Δ*vioE* against *C. albicans* SC5314 demonstrated equivalent inhibitory activity between the two strains (Figure 11A). *C. albicans* growth area in the presence of Δ*vioE* volatile emissions was reduced by 83.6% relative to control (mean ± SD: 11,588 ± 5,683 vs. 70,492 ± 38,729 pixels), compared to 90.0% reduction for wild-type BUC-1 (7,025 ± 8,367 pixels)- also showing no statistically significant difference between one another ($p > 0.05$). The difference in fungal colony counts exposed to the two bacteria was not statistically significant ($p = 0.30$, independent samples t-test; Figure 11B).

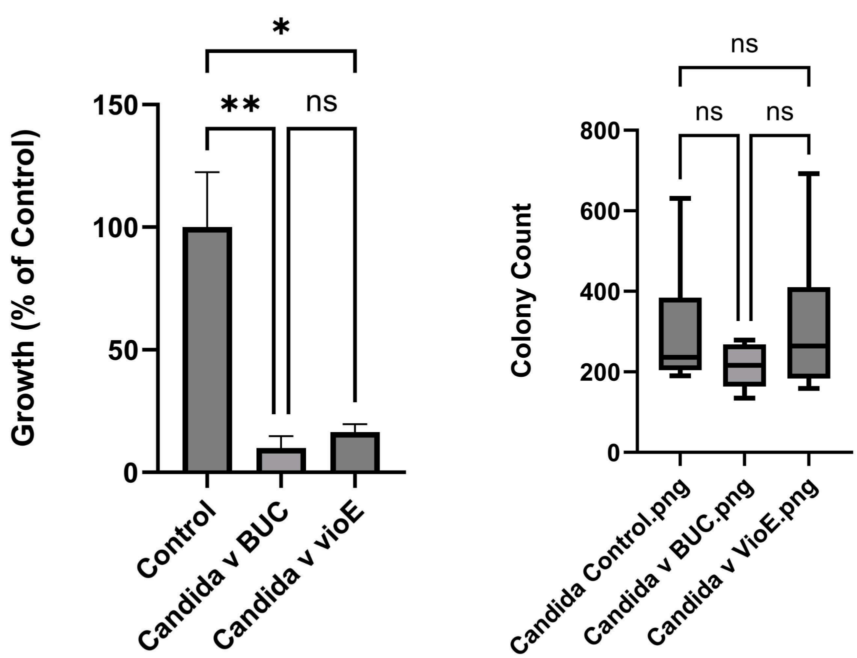

Figure 11. ***C. albicans*** **growth and colony counts following volatile exposure to BUC-1 WT and BUC-1 ΔvioE. (A)** ***C. albicans*** **SC5314 growth area expressed as a percentage of the no-bacteria control following 48 hours of volatile co-incubation at 30°C. No significant difference in inhibitory activity between BUC-1 WT and BUC-1 ΔvioE (p = 0.30); both conditions produced significantly reduced fungal growth relative to control (p = 0.003 and p = 0.004, respectively). (B)** ***C. albicans*** **colony counts following volatile exposure to BUC-1 WT and BUC-1 ΔvioE. No significant difference between strains (p = 0.30); both conditions showed significantly reduced colony counts relative to control (p = 0.003 and p = 0.004, respectively).**

CviR Is Required for Full Volatile-Mediated Inhibitory Activity in BUC-1

Having established that the volatile inhibitory activity of BUC-1 is independent of violacein, attention was directed toward the regulatory mechanisms governing VOC production. The CviIR quorum sensing system coordinates gene expression in *Chromobacterium* species in response to cell density, and the *cvi*R gene encodes the LuxR-type transcriptional regulator that served as the proximal activator of QS-regulated secondary metabolic gene expression. To test whether CviR-mediated regulation is required for the expression of the antifungal VOC phenotype, a chromosomal insertion mutant of *cvi*R was constructed in BUC-1 as described in Materials and Methods. Disruption of *cvi*R was confirmed by PCR, and the mutant, much like the previous, does not exhibit any affected behaviour in terms of growth rate, colony morphology, and motility, indicating that the insertion did not impose any apparent general fitness cost.

Volatile exposure assays comparing BUC-1 wild-type and BUC-1 Δ*cvi*R against *C. albicans* SC5314 revealed a marked and statistically significant attenuation of inhibitory activity in the *cvi*R mutant (Figure 12A). Whereas wild-type BUC-1 reduced *C. albicans* growth area to 3.2% of the no-bacteria control level (mean ± SD: 2,168 ± 1,913 vs. 67,744 ± 26,542 pixels; 96.8% inhibition), exposed individuals to the Δ*cvi*R mutant retained 68.6% of control growth area (46,490 ± 18,513 pixels; only 31.4% inhibition). Notably, the Δ*cvi*R-exposed growth area was not statistically distinguishable from the no-bacteria control (p = 0.07, independent samples t-test), indicating near-complete loss of volatile inhibitory activity. The difference between wild-type and Δ*cvi*R was highly significant ($p < 0.001$; Mann–Whitney U $p = 0.0004$; Figure 12B). Quantification of *C. albicans* percent growth across all conditions — including no-bacteria control, BUC-1 wild-type exposure, and BUC-1 Δ*cvi*R exposure — confirmed that *cvi*R disruption enables statistically significant levels of fungal growth due to loss of volatile inhibitory activity.

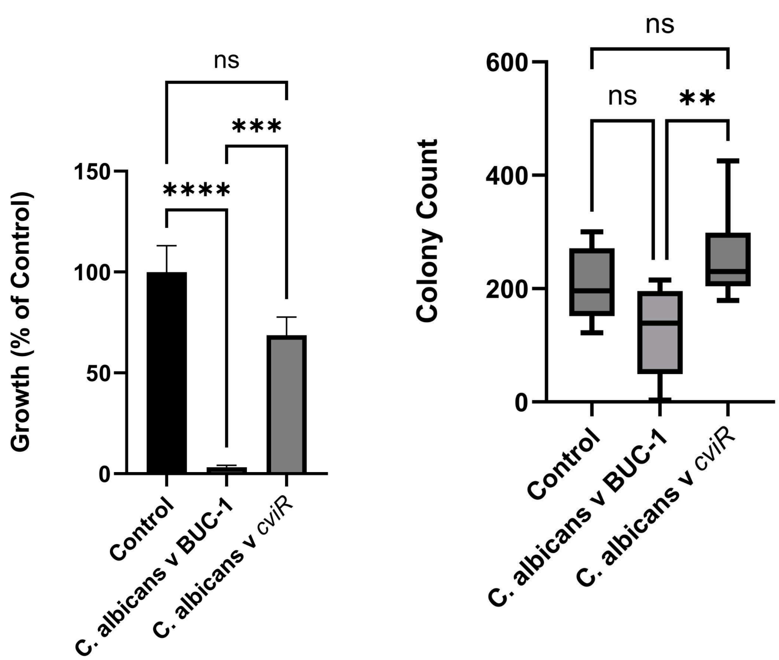

Figure 12. ***C. albicans*** **growth and colony counts following volatile exposure to BUC-1 WT and BUC-1 ΔcviR. (A)** ***C. albicans*** **SC5314 growth area expressed as a percentage of the no-bacteria control following 48 hours of volatile co-incubation at 30°C. BUC-1 WT produced near-complete suppression of fungal growth relative to control ($p < 0.001$); BUC-1 ΔcviR was not significantly different from the no-bacteria control ($p = 0.07$), and differed significantly from BUC-1 WT ($p < 0.001$; Mann–Whitney U $p = 0.0004$). (B)** ***C. albicans*** **colony counts comparing no-bacteria control, BUC-1 WT, and BUC-1 ΔcviR. BUC-1 WT and ΔcviR differ significantly ($p < 0.001$). ΔcviR is not significantly different from control ($p = 0.07$).**

Exogenous AHL Addition Does Not Rescue the ΔcviR Mutant Inhibitory Phenotype

To further confirm the specificity of the *cvi*R gene product in the regulatory cascade governing antifungal VOC emission, an autoinducer rescue experiment was performed. The rationale was as follows: if the attenuated phenotype of the Δ*cvi*R mutant is due to loss of the CviR receptor — which is required to transduce the AHL signal into transcriptional activation of downstream VOC biosynthesis genes — then supplying exogenous C6-HSL autoinducer to the mutant culture should not restore inhibitory activity, since the receptor is absent and the signal cannot be transduced. By contrast, if the attenuated phenotype were instead attributable to a mistaken mutation that has insufficient endogenous AHL production (i.e., a *cviI*-like defect), exogenous AHL supplementation would be expected to at least partially restore the phenotype.

Supplementation of BUC-1 Δ*cvi*R cultures with exogenous C6-HSL at the concentrations tested did not restore volatile-mediated inhibitory activity against *C. albicans*, nor did it affect fungal colony viability (Figure 13). The absence of phenotypic rescue is fully consistent with the expected consequence of *cvi*R disruption: without the receptor protein, the autoinducer signal cannot be transduced regardless of its extracellular concentration. It should be noted that the ideal positive control for an autoinducer rescue experiment of this design is a Δ*cviI* autoinducer synthase mutant, which retains a functional CviR receptor and would therefore be expected to respond to exogenous C6-HSL supplementation; such a strain is not currently available in this laboratory and represents a priority target for future work.

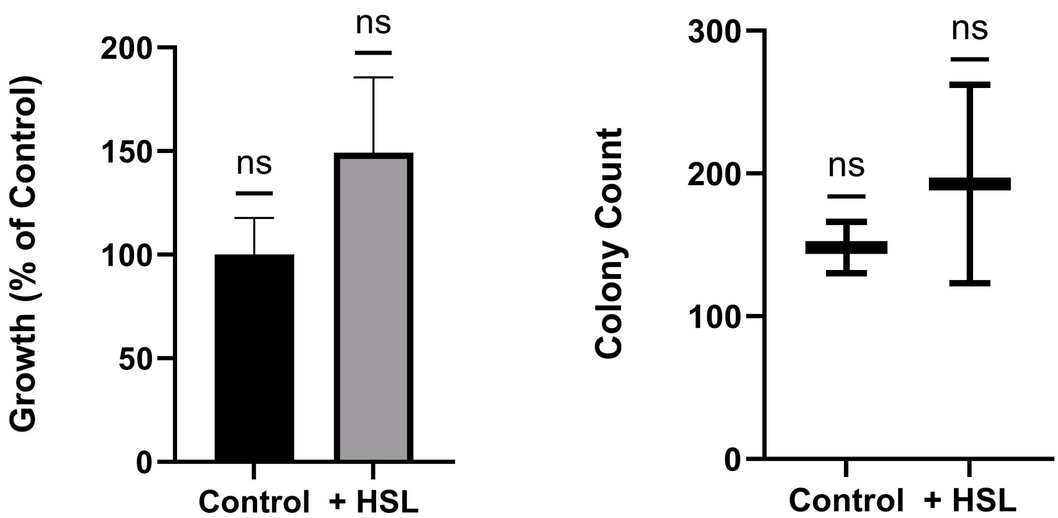

Figure 13. AHL rescue experiment: effect of exogenous C6-HSL supplementation on BUC-1 Δ*cviR* volatile inhibitory activity. (A) *C. albicans* SC5314 growth area expressed as a percentage of the no-bacteria control after 48 hours of volatile co-incubation with BUC-1 Δ*cviR* on KMB agar without or with agar-incorporated 10 µM C6-HSL. AHL supplementation does not restore volatile inhibitory activity to the Δ*cviR* mutant; neither condition differs significantly from one another (ns for both). (B) *C. albicans* colony counts from the same experiment. No significant difference between Δ*cviR* and Δ*cviR* + C6-HSL conditions (ns).

2, 3-DMCA Treatment Suppresses CviR-Regulated Outputs and Attenuates Volatile Antifungal Activity

To provide chemical validation of the genetic findings, BUC-1 cultures were exposed to 2,3-dimethoxycinnamic acid (2,3-DMCA) at 3,230 µM — a concentration selected to achieve near-complete suppression of CviR-regulated violacein output while remaining within the compound's established viability window for *C. violaceum* (41). Three conditions were established in parallel: BUC-1 without 2,3-DMCA, BUC-1 with 2,3-DMCA, and a bacteria-free 2,3-DMCA control. The bacteria-free 2,3-DMCA control confirmed that the compound exerts no direct antifungal activity against *C. albicans* at this concentration, producing fungal growth indistinguishable from the no-bacteria atmospheric control, and establishing that any attenuation of inhibitory activity observed in the BUC-1 + 2,3-DMCA condition is attributable to disruption of bacterial QS output rather than chemical action on the fungus.

Violacein production was quantified as the primary readout of CviIR regulon activity, as it is a well-established CviR-regulated output whose measurement by ethanol extraction and OD_{575} absorbance provides a reliable proxy for overall QS-regulated secondary metabolite production. Across three independent biological runs ($n = 9$ wells per condition), 2,3-DMCA treatment produced a dramatic and consistent suppression of violacein output. Normalized violacein (OD_{575}/OD_{600}) was reduced by 85.9% in treated cultures relative to untreated controls (control: 1.047 ± 0.073; treated: 0.147 ± 0.045; $p < 0.001$, t-test; Mann–Whitney U $p < 0.001$), with highly consistent suppression observed across all three independent runs (83.5%, 88.0%, and 86.2% per run; Figure 14B). Drip-plate viability counts confirmed that this concentration is neither bactericidal nor bacteriostatic: colony-forming unit counts were not significantly different between treated and untreated cultures in any run (Run 1: $p = 0.47$; Run 2: $p = 0.18$; Run 3: $p = 0.62$; Figure 14C), confirming that the reduction in QS output reflects transcriptional suppression rather than growth inhibition.

The functional consequence of CviR regulon suppression was a substantial and statistically significant attenuation of volatile antifungal activity against *C. albicans* (Figure 14A). In the untreated condition, BUC-1 volatile emissions restricted fungal growth to 4.61% of the no-bacteria atmospheric control, a 95.4% inhibition consistent with the potent inhibitory phenotype established across prior experiments. In the presence of 2,3-DMCA at 3,230 μM, this inhibitory activity was substantially reduced: *C. albicans* growth recovered to 42.89% of the atmospheric control (57.1% inhibition), representing a 9.3-fold increase in fungal proliferation relative to the untreated BUC-1 condition ($p < 0.001$). Critically, pairwise comparisons among all three conditions were highly significant: the untreated BUC-1 condition differed from both the atmospheric control and the 2,3-DMCA-treated condition ($p < 0.001$ for both), and the DMCA-treated condition remained significantly below the no-bacteria control ($p < 0.001$), indicating that the partially suppressed QS state still produces enough volatile output to exert measurable antifungal pressure.

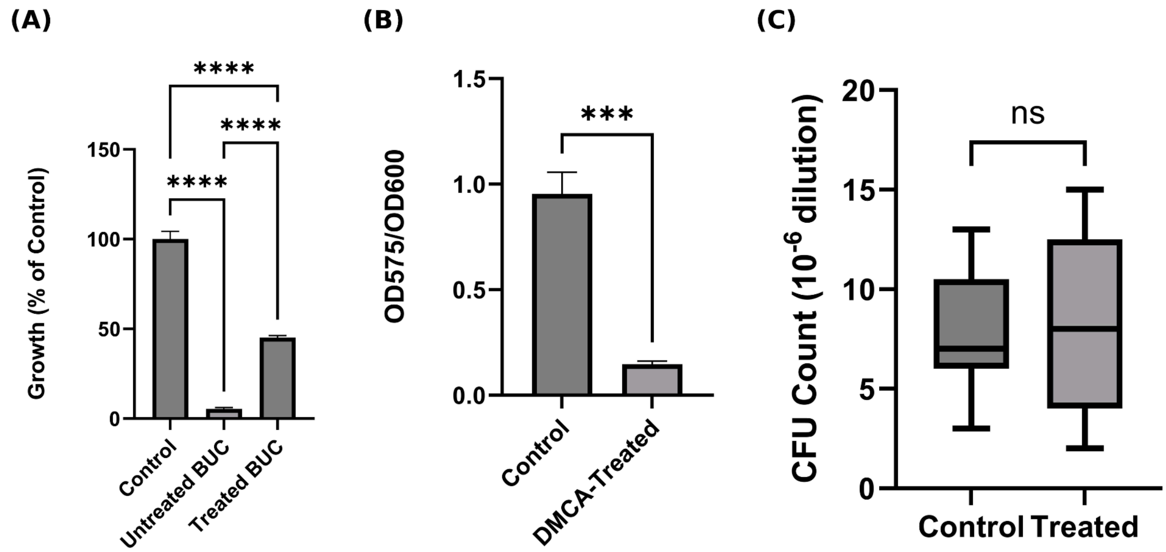

Figure 14. 2,3-DMCA quorum sensing disruption experiment. (A) *C. albicans* growth area (% of control) for untreated and DMCA-treated BUC-1 conditions. (B) Normalized violacein production (OD575/OD600) confirming 85.9% suppression of CviR-regulated output ($p < 0.001$). (C) CFU counts confirming bacterial viability is unaffected by DMCA treatment (ns).

The degree of volatile inhibitory activity recovered under 2,3-DMCA treatment is informative when placed in direct comparison to the ΔcviR genetic disruption result. The Δ*cvi*R mutant, which constitutively silences the entire CviR regulon, permitted fungal growth to 68.6% of the no-bacteria control (31.4% inhibition). The 2,3-DMCA-treated condition, by contrast, permitted growth to only 42.89% of control (57.1% inhibition), retaining substantially more inhibitory activity than the genetic deletion despite an 85.9% reduction in the CviR-regulated violacein output. This 25.7 percentage point difference between the two perturbation outcomes reflects the mechanistic distinction between complete receptor disruption and partial chemical suppression: while the Δ*cvi*R strain produces no CviR-dependent transcription regardless of autoinducer levels, 2,3-DMCA achieves competitive but incomplete receptor occupancy, leaving a residual fraction of CviR-regulated gene expression intact. The VOCs produced under this residual activity continue to accumulate in the shared environment throughout the 48-hour co-incubation, and their cumulative concentration is sufficient to produce inhibitory outcomes exceeding what is observed when CviR is eliminated entirely. Together, the magnitude of *Candida* growth recovery (9.3-fold relative to untreated BUC-1), the significance of all three pairwise comparisons, and the systematic concordance between violacein suppression and antifungal attenuation provide convergent pharmacological evidence that volatile-mediated antifungal activity in BUC-1 is a CviR-regulated output.

Discussion

The results presented in this chapter establish that the volatile-mediated antifungal activity of *Chromobacterium vaccinii* BUC-1 against *Candida albicans* is regulated by the CviIR quorum sensing system and is produced independently of violacein. Four lines of experimental evidence converge on this conclusion: the equivalence of *C. subtsugae* pigment-producing and pigment-null strains in the volatile inhibition assay, alongside the unchanged inhibitory activity of the BUC-1 Δ*vioE* mutant; the pharmacological disruption by 2,3-DMCA produces a consistent and substantial suppression of CviR-regulated secondary metabolite production without eliminating cell viability; the marked attenuation of inhibition in the BUC-1 ΔcviR mutant; and the failure of exogenous AHL to rescue the ΔcviR phenotype. Together, these findings identify CviR-dependent transcriptional regulation as a necessary component of the molecular pathway leading to antifungal VOC emission.

Violacein Is Not the Active Volatile Antifungal Agent

The literature on *C. violaceum* has demonstrated that purified violacein and violacein-producing culture supernatants inhibit a broad range of fungal species in vitro [42–44], leading to the hypothesis that violacein might also contribute to volatile-phase inhibition. The present data refute this hypothesis through two independent experimental approaches. *C. subtsugae* pigment-producing and pigment-null strains produced statistically equivalent reductions in *C. albicans* growth area (84.5% and 80.9% respectively; $p = 0.44$), and BUC-1 Δ*vioE* produced equivalent inhibition to wild-type BUC-1 (83.6% vs. 90.0%; $p = 0.30$). These findings are in accordance with the physical and chemical properties of violacein, whose large, complex structure and low vapor pressure make it an unlikely candidate for the transition into the volatile phase under standard laboratory or environmental conditions. So, these results across two organisms and two independent approaches to eliminating violacein production provides strong evidence that the active volatile agent is independent of the violacein biosynthesis pathway.

The use of *C. subtsugae*, a strain reclassified from the originally reported *C. violaceum* ATCC 12472 [40], is appropriate here because its QS system and violacein biosynthesis pathway are well characterized and broadly comparable to those of *C. violaceum*, making it a suitable organism in which to examine the consequences of violacein absence for volatile antifungal activity. The equivalence of this variant and the pigment-producing parent in the volatile assay indicates that violacein biosynthesis genes are dispensable for antifungal VOC emission in this species. The BUC-1 Δ*vioE* mutant result confirms and extends this conclusion to the primary strain of interest, and the specificity of the *vioE* disruption — targeting only the terminal enzyme of the violacein pathway — minimizes the likelihood of unwanted effects on downstream genes unrelated to pigmentation. The consistency of these results across two different *Chromobacterium* species and two different approaches to halting violacein production provides strong evidence that the antifungal volatile activity resides in a chemically distinct class of VOCs whose production does not depend on violacein biosynthesis, not accounting for the well-documented antibacterial and antifungal contact activity of violacein itself [42–44].

CviR-Dependent Quorum Sensing Regulates Antifungal VOC Production

The marked attenuation of volatile inhibitory activity in the BUC-1 Δ*cvi*R mutant — from 96.8% growth area inhibition in wild-type to only 31.4% in the mutant, with the mutant's growth area statistically indistinguishable from the uninhibited control ($p = 0.07$) — establishes CviR as a required regulatory component of the antifungal VOC phenotype. This finding is consistent with the known role of LuxR-type transcriptional regulators as master regulators of secondary metabolite production in Gram-negative bacteria: by integrating population density information encoded in extracellular AHL concentration, CviR coordinates the expression of metabolic gene clusters at the population level [25,45], ensuring that energetically costly secondary metabolite production is initiated only when cell density is sufficient to produce a physiologically meaningful outcome. *Chromobacterium* species have long served as models for studying the consequences of QS disruption on social behavior and secondary metabolite production, and disrupting quorum sensing in *C. violaceum* has been demonstrated to substantially alter colony-level social interactions and pigment production [24]. The present results suggest that the antifungal VOC biosynthesis machinery is among the gene sets under CviR control in *C. vaccinii* BUC-1.

The residual inhibitory activity retained by the ΔcviR mutant warrants interpretive consideration. The incomplete abolition of inhibition suggests that CviR-independent pathways possibly contribute to VOC production, potentially including constitutively expressed volatile biosynthesis genes or other regulatory circuits that are partially redundant with the CviIR system. This represents an important direction for future investigation. Whether these genes constitute a known component of the CviR regulon or represent a previously uncharacterized target gene set within the as-yet undefined global CviIR regulon remains an open question. Resolving this question will require transcriptomic profiling comparing wild-type BUC-1 and the Δ*cvi*R mutant under VOC-inducing conditions, an approach identified as a priority future direction in Chapter 4.

AHL Non-Rescue Confirms Receptor-Level Disruption

The failure of exogenous C6-HSL to restore inhibitory activity to the ΔcviR mutant is mechanistically informative beyond simply confirming the receptor-level nature of the disruption. The *cvi*R insertion renders the cell constitutively oblivious to quorum sensing input: without a functional receptor, the autoinducer signal cannot be perceived, and the full downstream transcriptional program under CviR control — including both canonical QS-regulated targets and non-canonical CviR regulon members — remains silenced regardless of environmental AHL concentration. A complementary genetic approach would be the construction and characterization of a ΔcviI autoinducer synthase mutant, which would serve as the proper positive control for AHL rescue experiments: unlike the receptor-null Δ*cvi*R strain, a synthase mutant retains an intact CviR receptor and its volatile inhibitory phenotype would therefore be expected to be rescued, at least partially, by exogenous C6-HSL supplementation. The absence of this strain currently limits the interpretive scope of the rescue experiment to confirming receptor-level disruption rather than formally demonstrating autoinducer sufficiency, and its construction is identified as a priority.

Chemical Validation of Quorum Sensing Dependence

The 2,3-DMCA experiment provides independent pharmacological support for the conclusion that CviR-mediated quorum sensing is required for antifungal VOC production. The rationale for employing a competitive antagonist of the autoinducer-binding domain as a pharmacological probe rests on a class of quorum sensing inhibitors whose structural basis for receptor antagonism was characterized in current literature [46], demonstrating that synthetic ligands occupying the autoinducer-binding pocket of LuxR-type receptors can act as potent antagonists by preventing the receptor from adopting the active conformation required for DNA binding, regardless of the endogenous autoinducer concentration present [46]. This strategy differs fundamentally from inhibitors that target autoinducer biosynthesis or stability, in that it acts at the level of signal reception rather than signal production [41,47].

The mechanism of action of 2,3-dimethoxycinnamic acid has been characterized in detail by Li et al. [41], who isolated the compound from the marine actinomycete *Nocardiopsis mentallicus* SCSIO 53858 and established it as a genuine quorum sensing inhibitor (QSI) rather than a conventional antibiotic: its minimum inhibitory concentration against *C. violaceum* exceeds 500 μg/mL, confirming that the effects observed at working concentrations are attributable to QS disruption rather than bacteriostatic or bactericidal growth inhibition- and setting the guidelines for the concentrations used in this study [41]. Molecular docking analysis demonstrated that 2,3-DMCA occupies the autoinducer-binding domain of the CviR receptor protein, positioning itself within the same binding cavity as the native C6-HSL ligand and competing with it through a combination of hydrogen bond interactions and hydrophobic contacts [41]. By displacing C6-HSL from the CviR binding pocket, 2,3-DMCA prevents the receptor from adopting the active conformation required for DNA binding and transcriptional activation of downstream target genes. Quantitative RT-PCR experiments confirmed that this competitive inhibition produces transcriptional suppression across multiple QS-regulated loci: treatment with 2,3-DMCA significantly reduced expression of *cvi*R itself, as well as *vioA*, *vioB*, and *vioE* — three genes encoding enzymes in the violacein biosynthesis pathway. At 150 µg/mL, 2,3-DMCA suppressed violacein production by 73.9%, swarming motility by 65.9%, and biofilm formation by 37.8%, consistent with broad silencing of the CviR regulon across multiple phenotypic outputs. The 85.9% reduction in normalized violacein (OD_{575}/OD_{600}) observed here across nine replicate wells is consistent with near-complete silencing of the CviIR regulon at 3,230 µM, closely mirroring the phenotype of the Δ*cvi*R insertion mutant. However, a direct quantitative comparison between the two perturbation outcomes reveals a mechanistically informative divergence. Whereas the Δ*cvi*R receptor- null mutant permitted fungal growth to 68.6% of the no-bacteria control, 2,3-DMCA-treated BUC-1 cultures permitted growth to only 42.89% of control, retaining 25.7 percentage points more inhibitory activity than the complete genetic disruption despite achieving near-equivalent suppression of the violacein reporter. This divergence is not paradoxical. Unlike receptor disruption, which constitutively silences all CviR-dependent transcription irrespective of autoinducer levels, competitive antagonism by 2,3-DMCA operates through occupancy of the autoinducer-binding domain and is subject to dynamic equilibrium with endogenous C6-HSL. At 3,230 µM, 2,3-DMCA reduces but does not eliminate CviR-dependent transcriptional output: the remaining ~14% of uninhibited regulon activity, inferred from the residual violacein production at 0.147 OD_{575}/OD_{600}, continues to drive VOC biosynthesis at a reduced rate. Because VOC-mediated antifungal activity is a gas-phase accumulative process rather than a contact-dependent one, even attenuated production allows volatile compounds to reach biologically relevant headspace concentrations over the course of a 48-hour co-incubation. The DMCA-treated condition therefore occupies a functionally intermediate state between wild-type and

Δ*cviR*: QS is substantially but incompletely silenced, VOC production is reduced but not eliminated, and the resulting antifungal effect is proportionally attenuated relative to wild-type while remaining meaningfully above the genetic null.

The functional consequence of QS suppression, a 9.3-fold increase in *C. albicans* growth relative to untreated BUC-1, confirms that volatile antifungal activity is a CviR-regulated output. The persistence of significant residual inhibition (42.89% of the no-bacteria control, compared to 100% in the uninhibited condition) is a direct consequence of the pharmacokinetic constraints of competitive QS antagonism in a volatile-output system. Because achieving complete CviR silencing through competitive displacement of C6-HSL is improbable without reaching concentrations that compromise bacterial viability, some fraction of receptor-dependent transcription invariably persists. The VOCs synthesized under this residual activity continue to diffuse into the sealed headspace throughout the co-incubation period, and such accumulation is sufficient to exert antifungal pressure well above the ΔcviR baseline. This makes the experimental dose a practical ceiling for pharmacological study of this phenotype: at lower 2,3-DMCA concentrations, the accelerated accumulation of VOCs from more complete QS activation would likely saturate the headspace inhibitory capacity before the end of the assay, collapsing the DMCA-treated condition toward the untreated BUC-1 outcome and obscuring the underlying QS dependence.

Two limitations of this experiment warrant acknowledgment. First, only a single working concentration of 2,3-DMCA was thoroughly evaluated. A dose-response series would establish whether there is a monotonic relationship between receptor occupancy and antifungal output attenuation, and would allow the approximate QS activity threshold required for volatile inhibitory activity to be estimated. Such data would significantly strengthen the pharmacological argument and is identified as a priority for future work. Second, DMSO was used as the solvent vehicle for

2,3-DMCA stock preparation, and the final DMSO concentration in experimental wells was approximately 3.2% v/v. Although a bacteria-free 2,3-DMCA control confirmed the absence of direct antifungal activity, a bacteria-containing DMSO-only control to verify that this solvent concentration does not independently affect BUC-1 QS activity or VOC production was not included in the current design. Future experimental iterations should incorporate this control explicitly. Within these limitations, the convergent evidence from the violacein quantification, the viability confirmation, and the functional *Candida* growth readout collectively support the conclusion that CviR-mediated quorum sensing is a necessary regulatory component of volatile antifungal output in BUC-1, and that this regulation is pharmacologically accessible through competitive antagonism of the autoinducer-binding domain.

Chapter 4: General Discussion and Conclusions

This thesis set out to address two connected problems: the mismatch of current image analysis tools' logic to the specific demands of plate-based microbial colony quantification, and the largely uncharacterized regulatory machinery governing volatile-mediated antifungal activity in *Chromobacterium vaccinii*. Both are highly dependent on one another. The credibility of the biological conclusions depends directly on the quality of the measurement tool being employed to produce them, and the practical significance of this tool is demonstrated by the biological question it enables.

The methodological foundation established in Chapter 2 addressed three specific failure modes identified in publicly available CellProfiler pipelines, specifically applied to petri dish imaging: the misclassification of noise through overreliance on intensity-based pixel identification logic primarily designed for mammalian cell microscopy workflows; the fragmentation of microbial colonies through shape-based declumping algorithms calibrated for eukaryotic cell compartments; and the absence of any filtering to prevent noise from passing through the analysis and exacerbating inflated colony counts and growth area. CAMP directly addressed these weaknesses through a transparent, modular structure of algorithms featuring two branches of thresholding, guided segmentation logic, and a redundant four to five descriptor morphological filter. The results presented a robust and significant improvement from current pipelines' performance: CAMP achieved a mean identification score nearly threefold greater than the most immediate comparable and relevant alternative pipeline, with a near-zero count bias of +1.5 colonies per image, species-invariant performance across both *Candida albicans* and *Staphylococcus aureus* species, and stable segmentation logic under all conditions.

The precision achieved by CAMP enabled the biological discoveries detailed in Chapter 3, which explored the regulatory control of antifungal volatile organic compounds (VOCs) in *C. vaccinii*.

Through multiple lines of genetic and pharmacological studies, this work established that the volatile-mediated inhibition of *Candida albicans* is independent of violacein and strictly requires a functional CviR quorum sensing receptor for significant activity. The equal inhibitory activity between wild-type and pigment-null mutants formally rules out violacein as the active agent, while the clear decrease in inhibition in the *∆cvi*R mutant identifies the CviR receptor as an essential regulatory agent for VOC production. Additionally, independent pharmacological confirmation of the antifungal VOC output as dependent on the CviR receptor is seen in the almost tenfold recovery of fungal growth under exposure to 2,3-DMCA-treated BUC-1. These findings identify quorum sensing as a primary intervention point for modulating bacterial VOC-mediated antifungal activity and narrow the chemical identity of the active compounds to the non-violacein fraction of CviR-regulated secondary metabolites.

This research opens up several avenues for future investigations for the broader scientific community to tackle. On the genetic side, the most immediate priority is the complementation and strengthening of the data found here with the addition of autoinducer mutant, Δ*cviI*, research in BUC-1. Unlike the receptor mutant , a synthase mutant retains an intact CviR receptor and would therefore be capable of responding to exogenous autoinducer, providing the positive control required to confidently demonstrate the role of the canonical quorum-sensing pathway in regulating the volatile-mediated activity of BUC-1. Additionally, it would provide the basis to carry out studies on the expression of autoinducer-independent levels of quorum-sensing, as suggested in current literature [48].

In parallel, transcriptomic profiling of BUC-1 wild-type versus the Δ*cvi*R mutant under VOC production conditions would identify the specific biosynthetic gene clusters subject to CviR-dependent activation, enabling targeted genetic dissection of the volatile pathway. The gene-level findings from transcriptomics would in turn guide the discovery of the molecular identity of the principal antifungal VOCs, work already underway in the Nau laboratory.

On the pharmacological side, the 2,3-DMCA experiments presented here were conducted at a single working concentration, which represents a methodological limit of the current study. A dose-response series would establish whether there is a monotonic relationship between CviR receptor occupancy and antifungal output, and would allow the approximate QS activity threshold required for volatile inhibitory activity to be estimated. Such data would substantially strengthen the pharmacological arm of this work and clarify the quantitative relationship between violacein suppression, used here as a proxy for overall regulon activity, and VOC production specifically.

On the translational side, the potential of chromobacterial volatile fractions warrants investigation not only as leads for antifungal drug discovery but also for applications outside of medicine, particularly in agriculture, where biological control of fungal pathogens represents a significant unmet need and where the gas-phase delivery mechanism of VOCs offers practical advantages over contact-dependent agents.

Two constraints of the current work should be acknowledged in finalizing these directions. The pharmacological characterization was conducted at a single compound concentration without a DMSO vehicle control, and the AHL rescue experiment lacks the Δ*cviI* positive control needed to demonstrate autoinducer sufficiency independently of receptor integrity. Both gaps are addressable through the targeted experiments identified above, and neither undermines the primary conclusion that CviR-dependent transcriptional regulation is required for volatile antifungal output.

Taken together, this work demonstrates that the translational gap in quantitative colony analysis can be meaningfully closed through principled pipeline architecture, and that the measurement precision resulting from this approach is capable of resolving the regulatory structure of a largely uncharacterized microbial competitive mechanism. The identification of quorum sensing as the primary regulatory driver governing volatile antifungal output in *C. vaccinii* positions this system as a genetically and pharmacologically relevant model for the broader investigation of bacterial VOC-mediated antifungal activity, with direct relevance to the search for novel agents against the priority fungal pathogens for which treatment options remain most severely limited.

Appendix

Appendix A - Representative Pipeline Output: Candida albicans Image 15492

Figure A1. CAMP output for Candida albicans image 15492 (F-factor = 0.796). Left: unadulterated plate image. Center: detected objects (white) on black background. Right: detection overlay on raw image (green outlines). CAMP correctly identifies the sparse, faint colonies on this low-density plate, with minor discrepancies due to annotation imperfection at colony peripheries.

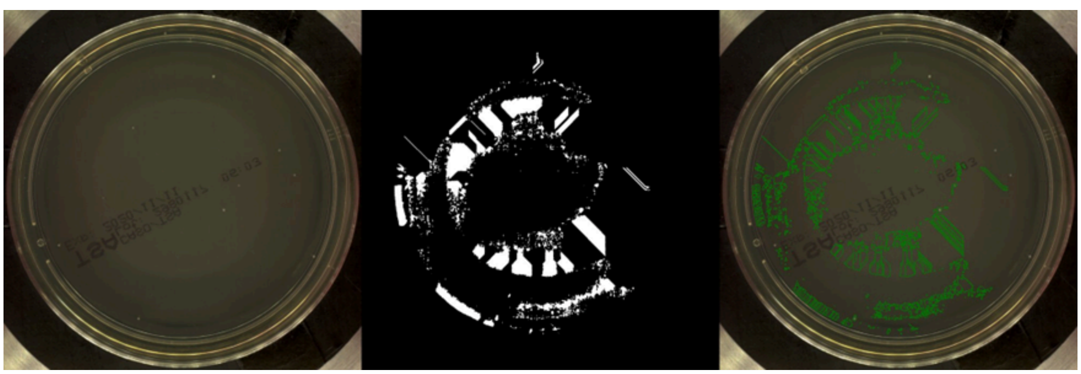

Figure A2. CellProfiler Template pipeline's output for Candida albicans image 15492 (F-factor = 0.008). Left: unadulterated plate image. Center: detected objects. Right: detection overlay. The pipeline detects no genuine colonies, instead producing fragmented detections at the plate rim consistent with density-dependent threshold collapse.

References

1. Carpenter AE, Jones TR, Lamprecht MR, Clarke C, Kang IH, Friman O, et al. CellProfiler: image analysis software for identifying and quantifying cell phenotypes. Genome Biol. 2006 Oct 31;7(10):R100. doi:10.1186/gb-2006-7-10-r100

2. Lamprecht MR, Sabatini DM, Carpenter AE. CellProfiler™: Free, Versatile Software for Automated Biological Image Analysis. BioTechniques. 2007 Jan 1;42(1):71–5. doi:10.2144/000112257 PubMed PMID: 17269487.

3. Stirling DR, Swain-Bowden MJ, Lucas AM, Carpenter AE, Cimini BA, Goodman A. CellProfiler 4: improvements in speed, utility and usability. BMC Bioinformatics. 2021 Sep 10;22(1):433. doi:10.1186/s12859-021-04344-9

4. WHO fungal priority pathogens list to guide research, development and public health action [Internet]. [cited 2026 Feb 24]. Available from: https://www.who.int/publications/i/item/9789240060241

5. Parambath S, Dao A, Kim HY, Zawahir S, Izquierdo AA, Tacconelli E, et al. Candida albicans-A systematic review to inform the World Health Organization Fungal Priority Pathogens List. Med Mycol. 2024 Jun 27;62(6):myae045. doi:10.1093/mmy/myae045 PubMed PMID: 38935906; PubMed Central PMCID: PMC11210619.

6. Bouz G, Doležal M. Advances in Antifungal Drug Development: An Up-To-Date Mini Review. Pharmaceuticals. 2021 Dec;14(12):1312. doi:10.3390/ph14121312

7. Ebadzadsahrai G, Higgins Keppler EA, Soby SD, Bean HD. Inhibition of Fungal Growth and Induction of a Novel Volatilome in Response to Chromobacterium vaccinii Volatile Organic Compounds. Front Microbiol. 2020;11:1035. doi:10.3389/fmicb.2020.01035 PubMed PMID: 32508802; PubMed Central PMCID: PMC7251293.

8. Bewes JM, Suchowerska N, McKenzie DR. Automated cell colony counting and analysis using the circular Hough image transform algorithm (CHiTA). Phys Med Biol. 2008 Oct;53(21):5991. doi:10.1088/0031-9155/53/21/007

9. Schneider CA, Rasband WS, Eliceiri KW. NIH Image to ImageJ: 25 years of image analysis. Nat Methods. 2012 Jul;9(7):671–5. doi:10.1038/nmeth.2089

10. Geissmann Q. OpenCFU, a New Free and Open-Source Software to Count Cell Colonies and Other Circular Objects. PLOS ONE. 2013 Feb 15;8(2):e54072. doi:10.1371/journal.pone.0054072

11. Clarke ML, Burton RL, Hill AN, Litorja M, Nahm MH, Hwang J. Low-cost, high-throughput, automated counting of bacterial colonies. Cytometry A. 2010;77A(8):790–7. doi:10.1002/cyto.a.20864

12. Jones TR, Kang IH, Wheeler DB, Lindquist RA, Papallo A, Sabatini DM, et al. CellProfiler Analyst: data exploration and analysis software for complex image-based screens. BMC Bioinformatics. 2008 Nov 15;9(1):482. doi:10.1186/1471-2105-9-482

13. Bray MA, Carpenter AE. CellProfiler Tracer: exploring and validating high-throughput, time-lapse microscopy image data. BMC Bioinformatics. 2015 Nov 4;16:368. doi:10.1186/s12859-015-0759-x PubMed PMID: 26537300; PubMed Central PMCID: PMC4634901.

14. Campbell L, Kumar M, Turner S. Using CellProfiler to Analyze and Quantify Vascular Morphology. In: de Lucas M, Etchhells JP, editors. Xylem: Methods and Protocols [Internet]. New York, NY: Springer; 2017 [cited 2026 Feb 24]. p. 179–89. Available from: https://doi.org/10.1007/978-1-4939-6722-3_13 doi:10.1007/978-1-4939-6722-3_13

15. Examples | CellProfiler [Internet]. [cited 2026 Feb 24]. Available from: https://cellprofiler.org/examples

16. Choudhry P. High-Throughput Method for Automated Colony and Cell Counting by Digital Image Analysis Based on Edge Detection. PLoS ONE. 2016 Feb 5;11(2):e0148469. doi:10.1371/journal.pone.0148469 PubMed PMID: 26848849; PubMed Central PMCID: PMC4746068.

17. Majchrowska S, Pawłowski J, Guła G, Bonus T, Hanas A, Loch A, et al. AGAR a microbial colony dataset for deep learning detection [Internet]. arXiv; 2021 [cited 2026 Apr 1]. Available from: http://arxiv.org/abs/2108.01234 doi:10.48550/arXiv.2108.01234

18. Pawłowski J, Majchrowska S, Golan T. Generation of microbial colonies dataset with deep learning style transfer. Sci Rep. 2022 Mar 25;12(1):5212. doi:10.1038/s41598-022-09264-z

19. Durán N, Menck CF. Chromobacterium violaceum: a review of pharmacological and industiral perspectives. Crit Rev Microbiol. 2001;27(3):201–22. doi:10.1080/20014091096747 PubMed PMID: 11596879.

20. Egorova DA, Voronina OL, Solovyev AI, Kunda MS, Aksenova EI, Ryzhova NN, et al. Integrated into Environmental Biofilm Chromobacterium vaccinii Survives Winter with Support of Bacterial Community. Microorganisms. 2020 Nov;8(11):11. doi:10.3390/microorganisms8111696

21. Johnson ET, Bowman MJ, Gomes RP, Carneiro LC, Dunlap CA. Identification of 2,4-diacetylphloroglucinol production in the genus Chromobacterium. Sci Rep. 2023 Aug 31;13(1):14292. doi:10.1038/s41598-023-41277-0

22. Kothari V, Sharma S, Padia D. Recent research advances on *Chromobacterium violaceum*. Asian Pac J Trop Med. 2017 Aug 1;10(8):744–52. doi:10.1016/j.apjtm.2017.07.022

23. Vöing K, Harrison A, Soby SD. Draft Genome Sequence of Chromobacterium vaccinii, a Potential Biocontrol Agent against Mosquito (Aedes aegypti) Larvae. Genome Announc. 2015 May 21;3(3):10.1128/genomea.00477-15. doi:10.1128/genomea.00477-15

24. Morohoshi T, Kato M, Fukamachi K, Kato N, Ikeda T. N-Acylhomoserine lactone regulates violacein production in Chromobacterium violaceum type strain ATCC 12472 [Internet]. [cited 2026 Mar 19]. Available from: https://dx.doi.org/10.1111/j.1574-6968.2007.01016.x

25. McClean KH, Winson MK, Fish L, Taylor A, Chhabra SR, Camara M, et al. Quorum sensing and Chromobacterium violaceum: exploitation of violacein production and inhibition for the detection of N-acylhomoserine lactones. Microbiol Read Engl. 1997 Dec;143 (Pt 12):3703–11. doi:10.1099/00221287-143-12-3703 PubMed PMID: 9421896.

26. De León ME, Wilson HS, Jospin G, Eisen JA. Genome sequencing and multifaceted taxonomic analysis of novel strains of violacein-producing bacteria and non-violacein-producing close relatives. Microb Genomics. 2023;9(4):000971. doi:10.1099/mgen.0.000971

27. Huang C, Chu X, Hui W, Xie C, Xu X. Study on extraction and characterization of new antibiotics violacein from engineered Escherichia coli VioABCDE-SD. Biotechnol Appl Biochem. 2023 Oct;70(5):1582–96. doi:10.1002/bab.2454 PubMed PMID: 36898961.

28. Devescovi G, Kojic M, Covaceuszach S, Cámara M, Williams P, Bertani I, et al. Negative Regulation of Violacein Biosynthesis in Chromobacterium violaceum. Front Microbiol. 2017 Mar 7;8. doi:10.3389/fmicb.2017.00349

29. Batista JH, da Silva Neto JF. Chromobacterium violaceum Pathogenicity: Updates and Insights from Genome Sequencing of Novel Chromobacterium Species. Front Microbiol. 2017 Nov 10;8. doi:10.3389/fmicb.2017.02213

30. Vasconcelos ATR de, de Almeida DF, Hungria M, Guimarães CT, Antônio RV, Almeida FC, et al. The Complete Genome Sequence of Chromobacterium violaceum Reveals Remarkable and Exploitable Bacterial Adaptability. Proc Natl Acad Sci U S A. 2003;100(20):11660–5.

31. Dodou HV, de Morais Batista AH, Sales GWP, de Medeiros SC, Rodrigues ML, Nogueira PCN, et al. Violacein antimicrobial activity on Staphylococcus epidermidis and synergistic effect on commercially available antibiotics. J Appl Microbiol. 2017 Oct;123(4):853–60. doi:10.1111/jam.13547 PubMed PMID: 28744944.

32. Batista AHM, Moreira ACD, de Carvalho RM, Sales GWP, Nogueira PCN, Grangeiro TB, et al. Antimicrobial Effects of Violacein against Planktonic Cells and Biofilms of Staphylococcus aureus. Molecules. 2017 Sep 25;22(10):1534. doi:10.3390/molecules22101534 PubMed PMID: 28946655; PubMed Central PMCID: PMC6151432.

33. Alves JA, Leal FC, Previato-Mello M, da Silva Neto JF. A Quorum Sensing-Regulated Type VI Secretion System Containing Multiple Nonredundant VgrG Proteins Is Required for Interbacterial Competition in Chromobacterium violaceum. Microbiol Spectr. 2022 Aug 31;10(4):e0157622. doi:10.1128/spectrum.01576-22 PubMed PMID: 35876575; PubMed Central PMCID: PMC9430734.

34. Soby SD, Gadagkar SR, Contreras C, Caruso FL. Chromobacterium vaccinii sp. nov., isolated from native and cultivated cranberry (Vaccinium macrocarpon Ait.) bogs and irrigation ponds. Int J Syst Evol Microbiol. 2013;63(Pt_5):1840–6. doi:10.1099/ijs.0.045161-0

35. Evans KC, Benomar S, Camuy-Vélez LA, Nasseri EB, Wang X, Neuenswander B, et al. Quorum-sensing control of antibiotic resistance stabilizes cooperation in Chromobacterium violaceum. ISME J. 2018 May 1;12(5):1263–72. doi:10.1038/s41396-018-0047-7

36. Deryabin DG, Inchagova KS, Nikonorova ER, Karimov IF, Duskaev GK. Quorum Sensing in Chromobacterium subtsugae ATCC 31532 (Formerly Chromobacterium violaceum ATCC 31532): Transcriptomic and Genomic Analyses. Microorganisms. 2025 May;13(5):1021. doi:10.3390/microorganisms13051021

37. Stauff DL, Bassler BL. Quorum Sensing in Chromobacterium violaceum: DNA Recognition and Gene Regulation by the CviR Receptor ▿. J Bacteriol. 2011 Aug;193(15):3871–8. doi:10.1128/JB.05125-11 PubMed PMID: 21622734; PubMed Central PMCID: PMC3147534.

38. Ravichandran V, Zhong L, Wang H, Yu G, Zhang Y, Li A. Virtual Screening and Biomolecular Interactions of CviR-Based Quorum Sensing Inhibitors Against Chromobacterium violaceum. Front Cell Infect Microbiol. 2018 Sep 4;8:292. doi:10.3389/fcimb.2018.00292 PubMed PMID: 30234025; PubMed Central PMCID: PMC6132053.

39. Pomianek ME, Semmelhack MF. Making Bacteria Behave: New Agonists and Antagonists of Quorum Sensing. ACS Chem Biol. 2007 May 1;2(5):293–5. doi:10.1021/cb700098c

40. Harrison AM, Soby SD. Reclassification of Chromobacterium violaceum ATCC 31532 and its quorum biosensor mutant CV026 to Chromobacterium subtsugae. AMB Express. 2020 Nov 7;10(1):202. doi:10.1186/s13568-020-01140-1

41. Li Y, Ding W, Yin J, Li X, Tian X, Xiao Z, et al. 2,3-Dimethoxycinnamic Acid from a Marine Actinomycete, a Promising Quorum Sensing Inhibitor in Chromobacterium violaceum. Mar Drugs. 2024 Apr;22(4):4. doi:10.3390/md22040177

42. Aruldass CA, Masalamany SRL, Venil CK, Ahmad WA. Antibacterial mode of action of violacein from Chromobacterium violaceum UTM5 against Staphylococcus aureus and methicillin-resistant Staphylococcus aureus (MRSA). Environ Sci Pollut Res Int. 2018 Feb;25(6):5164–80. doi:10.1007/s11356-017-8855-2 PubMed PMID: 28361404.

43. Wang H, Wang F, Zhu X, Yan Y, Yu X, Jiang P, et al. Biosynthesis and characterization of violacein, deoxyviolacein and oxyviolacein in heterologous host, and their antimicrobial activities. Biochem Eng J. 2012 Aug 15;67:148–55. doi:10.1016/j.bej.2012.06.005

44. Matz C, Deines P, Boenigk J, Arndt H, Eberl L, Kjelleberg S, et al. Impact of violacein-producing bacteria on survival and feeding of bacterivorous nanoflagellates. Appl Environ Microbiol. 2004 Mar;70(3):1593–9. doi:10.1128/AEM.70.3.1593-1599.2004 PubMed PMID: 15006783; PubMed Central PMCID: PMC368400.

45. Galloway WRJD, Hodgkinson JT, Bowden SD, Welch M, Spring DR. Quorum Sensing in Gram-Negative Bacteria: Small-Molecule Modulation of AHL and AI-2 Quorum Sensing Pathways. Chem Rev. 2011 Jan 12;111(1):28–67. doi:10.1021/cr100109t

46. Chen G, Swem LR, Swem DL, Stauff DL, O'Loughlin CT, Jeffrey PD, et al. A Strategy for Antagonizing Quorum Sensing. Mol Cell. 2011 Apr 22;42(2):199–209. doi:10.1016/j.molcel.2011.04.003

47. Blosser R, Gray K. Extraction of violacein from Chromobacterium violaceum provides a new quantitative bioassay for N-acyl homoserine lactone autoinducers. J Microbiol Methods. 2000 Apr 1;40:47–55. doi:10.1016/S0167-7012(99)00136-0

48. Batista BB, de Lima VM, Picinato BA, Koide T, da Silva Neto JF. A quorum-sensing regulatory cascade for siderophore-mediated iron homeostasis in Chromobacterium violaceum. mSystems. 9(4):e01397-23. doi:10.1128/msystems.01397-23 PubMed PMID: 38501880; PubMed Central PMCID: PMC11019928.